



Originally published as:

Tanaka, Y., Hasegawa, T., Tsuruoka, H., Klemann, V., Martinec, Z. (2015): Spectral-finite element approach to post-seismic relaxation in a spherical compressible Earth: application to gravity changes due to the 2004 Sumatra-Andaman earthquake. - *Geophysical Journal International*, 200, p. 299-321

DOI: <http://doi.org/10.1093/gji/ggu391>

# Spectral-finite element approach to post-seismic relaxation in a spherical compressible Earth: application to gravity changes due to the 2004 Sumatra–Andaman earthquake

Y. Tanaka,<sup>1</sup> T. Hasegawa,<sup>2</sup> H. Tsuruoka,<sup>3</sup> V. Klemann<sup>4</sup> and Z. Martinec<sup>5,6</sup>

<sup>1</sup>*Division of Monitoring Geoscience, Earthquake Research Institute, University of Tokyo, 1-1-1 Yayoi, Bunkyo-ku, Tokyo 113-0032, Japan.*

*E-mail: y-tanaka@eri.u-tokyo.ac.jp*

<sup>2</sup>*Department of Geophysics, Kyoto University, Kitashirakawa Oiwake-cho, Sakyo-ku, Kyoto 606-8502, Japan*

<sup>3</sup>*Earthquake and Volcano Information Center, Earthquake Research Institute, University of Tokyo, 1-1-1 Yayoi, Bunkyo-ku, Tokyo 113-0032, Japan*

<sup>4</sup>*Section 1.3: Earth System Modelling, GFZ German Research Centre for Geosciences, Telegrafenberg, D-14473 Potsdam, Germany*

<sup>5</sup>*Geophysics Section, School of Cosmic Physics, Dublin Institute for Advanced Studies, 5 Merriam Square, Dublin 2, Ireland*

<sup>6</sup>*Department of Geophysics, Charles University, V Holešovičkách 2, 180 00 Prague 8, Czech Republic*

Accepted 2014 October 7. Received 2014 October 7; in original form 2014 January 27

## SUMMARY

Global navigation satellite systems (GNSSs) have revealed that a mega-thrust earthquake that occurs in an island-arc trench system causes post-seismic crustal deformation. Such crustal deformation data have been interpreted by combining three mechanisms: afterslip, poroelastic rebound and viscoelastic relaxation. It is seismologically important to determine the contribution of each mechanism because it provides frictional properties between the plate boundaries and viscosity estimates in the asthenosphere which are necessary to evaluate the stress behaviour during earthquake cycles. However, the observation sites of GNSS are mostly deployed over land and can detect only a small part of the large-scale deformation, which precludes a clear separation of the mechanisms. To extend the spatial coverage of the deformation area, recent studies started to use satellite gravity data that can detect long-wavelength deformations over the ocean. To date, compared with theoretical models for calculating the post-seismic crustal deformation, a few models have been proposed to interpret the corresponding gravity variations. Previous approaches have adopted approximations for the effects of compressibility, sphericity and self-gravitation when computing gravity changes. In this study, a new spectral-finite element approach is presented to consider the effects of material compressibility for Burgers viscoelastic earth model with a laterally heterogeneous viscosity distribution. After the basic principles are explained, it is applied to the 2004 Sumatra–Andaman earthquake. For this event, post-seismic deformation mechanisms are still a controversial topic. Using the developed approach, it is shown that the spatial patterns of gravity change generated by the above three mechanisms clearly differ from one another. A comparison of the theoretical simulation results with the satellite gravity data obtained from the Gravity Recovery and Climate Experiment reveals that both afterslip and viscoelastic relaxation are occurring. Considering the spatial patterns in satellite gravity fields is an effective method for investigating post-seismic deformation mechanisms.

**Key words:** Satellite geodesy; Satellite gravity; Transient deformation; Time variable gravity; Subduction zone processes; Rheology: mantle.

## 1 INTRODUCTION

Large-scale co- and post-seismic crustal deformations due to mega-thrust earthquakes have been detected by the global navigation satellite systems (GNSSs; Dow *et al.* 2009) such as the 2004 Sumatra–Andaman, the 2010 Maule and the 2011 off the Pacific Coast of Tohoku events (e.g. Hashimoto *et al.* 2006; Ozawa *et al.* 2011; Vigny *et al.* 2011). It is well known that coseismic crustal deformation

can be explained by an elastic theory of dislocation (e.g. Okada 1985), whereas different mechanisms have been proposed to interpret post-seismic deformation. To identify the mechanisms of post-seismic deformation is important because it reveals the frictional, viscoelastic and poroelastic properties of a plate subduction boundary (e.g. Sholz 1998; Barbot & Fialko 2010). These properties are necessary to infer the stress behaviour in earthquake cycles (e.g. Wang *et al.* 2012a).

There are three mechanisms representing post-seismic deformation: (1) afterslip is considered to explain the relatively short-term deformation that occurs during the first few years after an earthquake. Afterslip is a slow fault slip and its space–time distribution can be inferred by a kinematic inversion of geodetic data based on an elastic dislocation theory. Afterslip usually occurs around the coseismic slip area (i.e. asperity; Ozawa *et al.* 2004), which is consistent with the frictional properties of rocks that have been confirmed by laboratory experiments (Sholz 1998). (2) Another mechanism to explain the short-term deformation is poroelastic rebound (e.g. Peltzer *et al.* 1998; Jonsson *et al.* 2003; Hughes *et al.* 2010). The coseismic deformation instantaneously creates a pressure gradient within the crust. Subsequently, transient fluid flow occurs along the pressure gradient, which results in transient crustal deformation. Usually, poroelastic rebound is dominant near the surface where groundwater is ample. However, recent findings suggest that poroelastic rebound (or diffusion of water) occurs also in the mantle (Ogawa & Heki 2007). (3) Longer-term crustal deformation that continues over several decades is considered to be driven by viscoelastic relaxation. In contrast to afterslip, this mechanism does not accompany a fault slip. The coseismic deformation yields a stress change in the viscously weak layers which are present in the lower crust and upper mantle. These stress changes relax gradually with time until new equilibrium state under the gravity field (i.e. isostasy) is reached which leads to a specific deformation field in the crust and mantle.

The deformations caused by each of these mechanism can be modelled and compared with observation data. It is common to combine more than one mechanism. The combination of afterslip and viscoelastic relaxation has been employed to explain crustal deformations caused by the large thrust-type events that occurred on plate subduction boundaries (e.g. Thatcher & Rundle 1984). For a shallower inland earthquake with a smaller magnitude, the three mechanisms can be separated relatively easily, because the coseismic deformation concentrates in the crust whereas the deformation in the asthenosphere is smaller and, so, viscoelastic relaxation tends to be less dominant. A typical surface deformation pattern that is caused by poroelastic rebound is opposite to that by afterslip, which can be effectively discerned by Interferometric Satellite Aperture Radar (InSAR; Jonsson *et al.* 2003; Barbot & Fialko 2010). However, great thrust-type earthquakes show a different behaviour. The epicentre is often surrounded by the ocean, where land observation sites cannot be deployed. The wavelength of the deformation tends to be larger than the size of the land, which precludes separation of spatial patterns. Consequently, it becomes difficult to separate the different mechanisms, for example when increasing the contribution of afterslip, that of viscoelastic relaxation must be decreased, and vice versa.

Satellite gravity data are useful when extending the spatial coverage for detecting the wide-range deformation caused by great earthquakes. The Gravity Recovery and Climate Experiment (GRACE) mission (Tapley *et al.* 2004) provides a monthly gravity change since 2002 with wavelengths greater than  $\sim 400$  km in the form of Stokes' coefficients. Although the temporal resolution of 1 month is lower than that of GNSS (1 d or shorter), the gravity variation is observed not only over the land but also at the ocean, with a precision of  $\sim 1 \mu\text{Gal}$  ( $=10^{-8}\text{ms}^{-2}$ ). Co- and post-seismic gravity variations have been identified using GRACE data (e.g. Han *et al.* 2006; Chen *et al.* 2007; de Linage *et al.* 2009; Matsuo & Heki 2011; Wang *et al.* 2012b). Mechanisms of post-seismic deformation by the 2004 Sumatra event have been discussed, using GNSS and GRACE data (e.g. Hashimoto *et al.* 2006; Pollitz *et al.* 2006; Chlieh *et al.*

2007; Ogawa & Heki 2007; Panet *et al.* 2007; Han *et al.* 2008; Hughes *et al.* 2010; Panet *et al.* 2010; Hoehner *et al.* 2011; Paul *et al.* 2012) where afterslip and viscoelastic relaxation are proposed as the dominant mechanism. Nevertheless, a consensus has not yet been reached regarding their respective contributions (see also Section 4) and while the accumulated effect up to present might be small for the 2010 Maule and the 2011 Tohoku events, most studies focused on the analysis of these events concentrate on afterslip.

In order to estimate large-scale post-seismic deformations with wavelengths greater than 100 km, the effects of self-gravitation and curvature of the Earth are not negligible (Sun & Okubo 1993). Therefore, many of the above-mentioned papers have calculated the deformation due to the 2004 Sumatra event with a spherical earth model (e.g. Sun & Okubo 1993; Pollitz 1997; Cambiotti *et al.* 2011). Effects of 3-D viscoelastic structures on displacement fields are also studied using a spherical model (Pollitz *et al.* 2008). Whereas in some studies (e.g. Piersanti *et al.* 1995; Pollitz 1997), terms representing the effects of compressibility and self-gravitation have been approximated, Tanaka *et al.* (2006, 2007) solved the governing equations without approximations which were already discussed by Peltier (1974) for a spherically symmetric viscoelastic structure by a different integration method. Similarly, Cambiotti *et al.* (2009) and Cambiotti & Sabadini (2010) calculated viscoelastic relaxation caused by a surface load for the same governing equations. Cambiotti *et al.* (2011) applied the method of Cambiotti *et al.* (2009) to the coseismic gravity variation caused by the 2004 Sumatra earthquake and showed that the vertical displacement and the resulting sea-level feedback could be reproduced when taking into account compressibility. Their method has not yet been applied to post-seismic deformation. Based on the theory of Martinec (2000), Tanaka *et al.* (2011) solved the surface-loading problem for a laterally heterogeneous viscosity distribution for a compressible continuum. In this spectral-finite element method, a finite-element representation is applied only in the radial direction, whereas the horizontal dependency is represented in a more analytical form based on tensor spherical harmonics. Because the deformation field is computed globally, the effects of curvature and self-gravitation are treated in a more natural manner. In the incompressible case, the same method has already been applied to calculate post-seismic relaxation (Tanaka *et al.* 2009). However, whether this method is valid for the compressible case has not yet been confirmed. Conventional finite-element methods are powerful tools that can consider effects including more complex heterogeneities in the material properties and geometry (e.g. Masterlark & Hughes 2008). However, due to the computational costs, deformation is not always solved globally, which causes an imbalance of gravitational effects, and artificial boundary conditions are usually added to avoid this imbalance (e.g. Cohen 1994; Wang *et al.* 2001; Hu *et al.* 2004). Conversely, the spectral-finite element approach does not consider the effects of laterally heterogeneous elasticity and density; instead, it treats the gravitational effects more accurately. Therefore, this approach is not only useful to calculate gravity changes that are suitable for comparison with satellite gravity data but also to confirm the accuracy of approximations for the effects of gravitation (and sphericity) in ordinary finite-element modelling. In addition, effects due to lateral heterogeneities in elasticity and density in such large-scale gravity field variations would be generally smaller than in the surface displacement fields. Fu & Sun (2008) reported that the effects of lateral heterogeneity of density on coseismic gravity changes are less than 1 per cent. However, viscosity in a subduction zone can change by at least one order of magnitude due to the presence of a slab. For an incompressible continuum the spectral-finite element method was

already applied by Klemann *et al.* (2007, 2008) in order to study the effect of lateral viscosity variations on surface displacement induced by glacial isostatic adjustment.

The aims of this study are as follows: in order to use GRACE data more effectively for separating the post-seismic deformation mechanisms, a calculation method that simultaneously considers sphericity, self-gravitation and a 3-D viscosity structure is necessary. To achieve this aim, the spectral-finite element method for the calculation of post-seismic deformations for the incompressible case (Tanaka *et al.* 2009) is extended to the compressible case (Section 2). Furthermore, to consider transient behaviour, also a Burgers rheology is incorporated. In order to show the validity of the developed method, separation of post-seismic deformation mechanisms is conducted for the 2004 Sumatra–Andaman event (Section 3). It will be particularly emphasized that, focusing on spatial patterns in GRACE gravity fields, facilitates to discern the effects due to after-slip and viscoelastic relaxation. Finally, the results are summarized and discussed in Section 4.

## 2 THEORY

### 2.1 Governing equations and boundary conditions

The differences that arise from introducing compressibility and the Burgers rheology appear in the constitutive law. The other processes including the numerical computation using the finite elements are the same as in the incompressible case with Maxwell rheology (Tanaka *et al.* 2009). Therefore, only the main points are outlined in this paper except for the constitutive law. For convenience, eq. (I-#) denotes eq. (#) in Tanaka *et al.* (2009).

The momentum and Poisson's equation for viscoelastic deformation of an initially hydrostatically prestressed self-gravitating sphere are given as

$$\operatorname{div} \boldsymbol{\tau} - \rho_0 \operatorname{grad} \phi_1 + \operatorname{div}(\rho_0 \mathbf{u}) \operatorname{grad} \phi_0 - \operatorname{grad}(\rho_0 \mathbf{u} \cdot \operatorname{grad} \phi_0) = 0, \quad (1)$$

$$\nabla^2 \phi_1 + 4\pi G \operatorname{div}(\rho_0 \mathbf{u}) = 0 \quad (2)$$

(e.g. Dahlen 1974) (the same as eqs I-1 and I-2), where  $\mathbf{u}$ ,  $\phi$ ,  $\boldsymbol{\tau}$  and  $G$  represent the displacement, the gravity potential increment, the stress tensor and Newton's gravitational constant, respectively,  $\rho_0 = \rho_0(r)$  is the initial density,  $r$  is the radial distance from the centre of the Earth, and the hydrostatic and perturbed states are expressed by the subscripts 0 and 1, respectively. In the earth model, the structure of elasticity and density is assumed to be spherically symmetric. The constitutive law for the compressible case is represented as

$$\dot{\boldsymbol{\tau}} = \dot{\boldsymbol{\tau}}^E - \frac{\mu}{\eta} \left( \boldsymbol{\tau} - \frac{1}{3} \operatorname{tr} \boldsymbol{\tau} \mathbf{I} \right), \quad (3)$$

$$\boldsymbol{\tau}^E = \lambda (\operatorname{div} \mathbf{u}) \mathbf{I} + 2\mu \boldsymbol{\epsilon}, \quad (4)$$

$$\boldsymbol{\epsilon} = \frac{1}{2} (\operatorname{grad} \mathbf{u} + \operatorname{grad}^T \mathbf{u}), \quad (5)$$

$$\frac{1}{3} \operatorname{tr} \boldsymbol{\tau} = K \operatorname{div} \mathbf{u} = \left( \lambda + \frac{2}{3} \mu \right) \operatorname{div} \mathbf{u}, \quad (6)$$

where  $\boldsymbol{\epsilon}$  represents the strain tensor and  $\lambda$ ,  $\mu$ ,  $K$  and  $\eta$  are Lamé's constants, the bulk modulus and the dynamic viscosity, respectively (Hanyk *et al.* 1995; Tanaka *et al.* 2011).

The constitutive law for a Burgers body is presented by Peltier (1981) as

$$\begin{aligned} \dot{\boldsymbol{\tau}} + A \left[ \boldsymbol{\tau} - \frac{1}{3} (\operatorname{tr} \boldsymbol{\tau}) \mathbf{I} \right] + B \left[ \boldsymbol{\tau} - \frac{1}{3} (\operatorname{tr} \boldsymbol{\tau}) \mathbf{I} \right] \\ = \lambda (\operatorname{div} \mathbf{u}) \mathbf{I} + 2\mu_1 \boldsymbol{\epsilon} + C \left[ \dot{\boldsymbol{\epsilon}} - \frac{1}{3} (\operatorname{div} \mathbf{u}) \mathbf{I} \right], \\ A = \frac{\mu_1 + \mu_2}{\eta_2} + \frac{\mu_1}{\eta_1}, \\ B = \frac{\mu_1 \mu_2}{\eta_1 \eta_2}, \\ C = \frac{2\mu_1 \mu_2}{\eta_2}, \end{aligned} \quad (7)$$

where a Maxwell and Kelvin–Voigt body are connected in series. There,  $\mu_1$  and  $\eta_1$  are shear modulus and the dynamic viscosity for the Maxwell element and  $\mu_2$  and  $\eta_2$  for the Kelvin–Voigt element, respectively. When  $\eta_2 = \infty$  and  $B = C = 0$ , the constitutive law for a Maxwell body is obtained (eqs 3–6). The rheological law in eq. (7) is only applied to the shear. The Burgers body exhibits a transient shear relaxation according to the Kelvin solid behaviour and a long-term Maxwell-fluid response, where the relaxation time of the transient Kelvin response ( $\eta_2/\mu_2$ ) is taken to be shorter than the steady-state relaxation time ( $\eta_1/\mu_1$ ; Pollitz 2003; Bürgmann & Dresen 2008). The bulk and shear modulus are the physically meaningful parameters describing elastic behaviour.

The boundary condition at the free surface ( $r = a$ ) is obtained by replacing a surface density with zero in the boundary condition for a surface load (sections 2.2–2.4 in Tanaka *et al.* 2011):

$$\begin{aligned} \boldsymbol{\tau} &= 0 \\ [\phi_1]_{\pm}^{\pm} &= 0 \\ [\operatorname{grad} \phi_1]_{\pm}^{\pm} \cdot \mathbf{e}_r + 4\pi G \rho_0^- (\mathbf{u}^- \cdot \mathbf{e}_r) &= 0, \end{aligned} \quad (8)$$

where the symbol  $[f]_{\pm}^{\pm}$  indicates the jump of quantity  $f$  on the free surface and a superscript  $+$  ( $-$ ) denotes the evaluation of  $f$  on the exterior (interior) side [I-(19)–(21)]. The boundary condition at the core–mantle boundary ( $r = b$ ) is also the same as for a surface load, which is given as

$$\begin{aligned} [\mathbf{u} \cdot \mathbf{n}]_{\pm}^{\pm} &= 0 \\ [\mathbf{n} \cdot \boldsymbol{\tau} \cdot \mathbf{n}]_{\pm}^{\pm} &= 0 \\ \boldsymbol{\tau} \cdot \mathbf{n} - (\mathbf{n} \cdot \boldsymbol{\tau} \cdot \mathbf{n}) &= 0, \end{aligned} \quad (9)$$

where  $\mathbf{n}$  is a unit vector normal to the interface. The inner core is ignored and an inviscid incompressible fluid core is assumed for  $r \leq b$ . The solution domain is restricted to  $b \leq r \leq a$  for reducing computational costs because deformations for shallower portions are more important in calculating post-seismic relaxation at the surface.

The boundary condition at the seismic source is formulated by double-couple forces equivalent to a point dislocation (section 2.2 of Tanaka *et al.* 2009). The representation of the source condition does not depend on the bulk modulus and coincides with the representation for the incompressible case. The Heaviside function is employed for the time variation of the dislocation. At the source, the given dislocation must be constant, which requires that the right-hand side of eq. (7) be zero. Because the boundary condition

is imposed in the form of double-couple forces, each force must attenuate with time as

$$\mathbf{f}^0 \exp[-(A^2 - \sqrt{A^2 - 4B})t]. \quad (10)$$

However, when the source is placed in the elastic lithosphere, this time variation is negligible ( $A = B = 0$ ).

## 2.2 Time-differencing scheme

In the governing equations, time derivatives appear only in the constitutive law. Defining the elastic part of the stress as  $\boldsymbol{\tau}^E = \lambda(\text{div}\mathbf{u})\mathbf{I} + 2\mu_1\boldsymbol{\epsilon}$  and applying the second-order explicit scheme (forward), the following time evolution formula is obtained:

$$\boldsymbol{\tau}^{i+1} = \boldsymbol{\tau}^{E,i+1} + \boldsymbol{\tau}^{V,i}, \quad (11)$$

$$\begin{aligned} \boldsymbol{\tau}^{V,i} = & \boldsymbol{\tau}^{V,i-1} + (1 - A\Delta t)(\boldsymbol{\tau}^{V,i-1} - \boldsymbol{\tau}^{V,i-2}) - B(\Delta t)^2 \boldsymbol{\tau}^{V,i-2} \\ & - 2\mu_1 A\Delta t \left[ \boldsymbol{\epsilon}^i - \boldsymbol{\epsilon}^{i-1} - \frac{1}{3} \text{div}(\mathbf{u}^i - \mathbf{u}^{i-1})\mathbf{I} \right] \\ & - 2\mu_1 B(\Delta t)^2 \left[ \boldsymbol{\epsilon}^{i-1} - \frac{1}{3} \text{div}\mathbf{u}^{i-1}\mathbf{I} \right] \\ & + C\Delta t \left[ \boldsymbol{\epsilon}^i - \boldsymbol{\epsilon}^{i-1} - \frac{1}{3} \text{div}(\mathbf{u}^i - \mathbf{u}^{i-1})\mathbf{I} \right], \end{aligned} \quad (12)$$

$$\Delta t = t^{i+1} - t^i, \quad (13)$$

$$\text{tr}\boldsymbol{\tau}^{V,i} = 0. \quad (14)$$

The choice of this differencing scheme simplifies the structure of the linear algebraic system associated with the elastic part of the deformation (the left-hand side of eq. 16), although the time step must be sufficiently small so that numerical stability is ensured [see section 3 in Martinec (2000) and Section 2.5 in this paper]. Due to the addition of the Kelvin–Voigt element, the viscous part of the stress at time step  $i$ ,  $\boldsymbol{\tau}^{V,i}$ , depends on the field variables at time step  $i - 2$ , and the coefficients of the strain and stress tensors differ from the case for the Maxwell body. Except from this, the above form is substantially the same as that for the Maxwell body. In particular, eq. (10) takes the same form as eq. (7) of Tanaka *et al.* (2011). By this similarity, the representation of the variation of the dissipative energy, which will be introduced later (i.e.  $\delta\mathcal{F}_{\text{diss}}$ ), remains unchanged from the case of surface loading (Tanaka *et al.* 2011). It follows that the computation code for the Burgers body can be obtained by only modifying the explicit time differencing scheme considered for the Maxwell body.

The initial value at  $t = 0$  or  $i = 0$  can be taken as

$$\begin{aligned} \boldsymbol{\tau}^0 &= \boldsymbol{\tau}^{E,0} \\ \boldsymbol{\tau}^{V,-1} &= 0 \\ \boldsymbol{\tau}^{V,0} &= -2\mu_1 A\Delta t (\boldsymbol{\epsilon}^0) + \frac{2\mu_1 A\Delta t}{3} (\text{div}\mathbf{u}^0)\mathbf{I} \\ &+ C\Delta t \left[ \boldsymbol{\epsilon}^0 - \frac{1}{3} (\text{div}\mathbf{u}^0)\mathbf{I} \right]. \end{aligned} \quad (15)$$

The first equation above implies that  $\boldsymbol{\epsilon}^0$  is equal to the instantaneous response to the Maxwell element, as  $\boldsymbol{\tau}^E$  does not include  $\mu_2$  and  $\eta_2$ . At  $t = 0$ , the viscous dissipation at the previous time step,  $\boldsymbol{\tau}^{V,-1}$ , is zero. It follows that the strain caused by a coseismic deformation,  $\boldsymbol{\epsilon}^0$ , is obtained by solving the force balance with double-couple forces represented in a weak form. Once a coseismic deformation is computed, the viscous dissipation at  $i = 0$  can be determined and considered in the next time step (eq. 11).

## 2.3 Weak formulation and energy functional

The viscoelastic deformation at each time step is obtained by solving the following variational equality in the weak formulation that consists of the energy functionals associated with the elastic deformation, self-gravitation and uniqueness of the solution and the linear functionals associated with the viscous dissipation and the boundary conditions (Martinec 2000):

$$\begin{aligned} \delta\mathcal{E}(\mathbf{u}^{i+1}, \phi_1^{i+1}, \delta\mathbf{u}, \delta\phi_1) &= \delta\mathcal{E}_{\text{bulk}}(\mathbf{u}^{i+1}, \delta\mathbf{u}) + \delta\mathcal{E}_{\text{shear}}(\mathbf{u}, \delta\mathbf{u}) \\ &+ \delta\mathcal{E}_{\text{grav}}(\mathbf{u}^{i+1}, \phi_1^{i+1}, \delta\mathbf{u}, \delta\phi_1) \\ &+ \delta\mathcal{E}_{\text{uniq}}(\mathbf{u}^{i+1}, \delta\mathbf{u}) \\ &= \delta\mathcal{F}_{\text{diss}}^i(\delta\mathbf{u}) + \delta\mathcal{F}_{\text{surf}}^{i+1}(\delta\mathbf{u}, \delta\phi_1) \\ &+ \delta\mathcal{F}_{\text{CMB}}^{i+1}(\delta\mathbf{u}, \delta\phi_1) \\ &+ \delta\mathcal{W}^{i+1}(\delta\mathbf{u}, \delta\phi_1), \end{aligned} \quad (16)$$

where  $i$  denotes the  $i$ th time step,  $\delta$  a variation and

$$\delta\mathcal{E}_{\text{bulk}}(\mathbf{u}^{i+1}, \delta\mathbf{u}) = \int_V \lambda(\text{div}\mathbf{u}^{i+1})(\text{div}\delta\mathbf{u}) dV,$$

$$\delta\mathcal{E}_{\text{shear}}(\mathbf{u}^{i+1}, \delta\mathbf{u}) = \int_V 2\mu(\boldsymbol{\epsilon}^{i+1} : \delta\boldsymbol{\epsilon}) dV,$$

where the symbol  $:$  denotes the double-dot product of tensors and  $\delta\boldsymbol{\epsilon}$  the strain tensor computed by the test function,  $\delta\mathbf{u}$ . The representation of the variations associated with the gravitational energy and the uniqueness of the solution is given in Martinec (2000).

The variation of the dissipation term on the right-hand side of the variational equality is represented as

$$\delta\mathcal{F}_{\text{diss}}^i(\delta\mathbf{u}) = - \int_V (\boldsymbol{\tau}^{V,i} : \delta\boldsymbol{\epsilon}) dV \quad (17)$$

and the variations for the interface conditions are

$$\begin{aligned} \delta\mathcal{F}_{\text{surf}}^{i+1}(\delta\mathbf{u}, \delta\phi_1) &= \frac{1}{4\pi G} \int_{\partial V} (\text{grad}\phi_1^+ \cdot \mathbf{e}_r) \delta\phi_1 dS \\ \delta\mathcal{F}_{\text{CMB}}^{i+1}(\delta\mathbf{u}, \delta\phi_1) &= \int_{\partial V} [\rho_c g_0(b)\mathbf{u} \cdot \delta\mathbf{u} \\ &+ \left( \frac{1}{4\pi G} \text{grad}\phi_1^- + \rho_c \mathbf{u} \right) \cdot \mathbf{e}_r \delta\phi_1] dS, \end{aligned} \quad (18)$$

where  $\rho_c$  and  $g_0(b)$  denote the density of the liquid core and the unperturbed gravitational acceleration at  $r = b$ , respectively, and  $\phi_1^{+(-)}$  is the perturbed gravitational potential on the exterior (interior) side of the interface at  $r = a(b)$  (Martinec 2000).  $\delta\mathcal{W}$  represents the contribution from a dislocation with an arbitrary mechanism (i.e. the moment magnitude and the dip, strike and rake angles; Tanaka *et al.* 2009).

## 2.4 Spectral-finite elements and evaluation of the dissipative energy

In the spectral-finite element method, the angular dependence of the field variables are decomposed by vector and scalar spherical harmonics, as follows:

$$\begin{aligned} \mathbf{u}^i(r, \theta, \varphi) &= \sum_{j=0}^{\infty} \sum_{m=-j}^j \left[ U_{jm}^i(r) \mathbf{S}_{jm}^{(-1)}(\theta, \varphi) + V_{jm}^i(r) \mathbf{S}_{jm}^{(1)}(\theta, \varphi) \right. \\ &\left. + W_{jm}^i(r) \mathbf{S}_{jm}^{(0)}(\theta, \varphi) \right], \\ \phi_1^i(r, \theta, \varphi) &= \sum_{j=0}^{\infty} \sum_{m=-j}^j F_{jm}^i(r) Y_{jm}(\theta, \varphi), \end{aligned} \quad (19)$$

where  $\theta$  and  $\varphi$  are the colatitude and longitude, respectively, and  $U_{jm}^i$  and  $V_{jm}^i$  denote the coefficients of the vertical and horizontal displacement at the  $i$ th time step for the spheroidal component with degree  $j$  and order  $m$ .  $W_{jm}^i$  represents the toroidal component. The definition of these spherical harmonics is given in appendix of Martinec (2000). The test functions are expanded in the same manner.

The radial dependence of the expansion coefficients is approximated by a linear combination of the piecewise linear base functions:

$$\begin{aligned} & [U_{jm}^i(r), V_{jm}^i(r), W_{jm}^i(r), F_{jm}^i(r)] \\ &= \sum_{k=1}^{P+1} [U_{jm}^{i,k}, V_{jm}^{i,k}, W_{jm}^{i,k}, F_{jm}^{i,k}] \psi_k(r), \end{aligned} \quad (20)$$

where  $P$  denotes the number of subintervals for  $b \leq r \leq a$ , and  $\rho_0(r)$ ,  $\lambda(r)$  and  $\mu(r)$  are approximated by piecewise constant functions such as  $\rho_0(r) = \rho_k$  for  $r_k \leq r < r_{k+1}$  (eqs 72 and 75 in Martinec 2000). The unperturbed gravitational acceleration at the  $k$ th radial interval is given as

$$g_0(r) = \frac{4\pi G}{3} \left[ \rho_k r + \sum_{i=2}^k (\rho_{i-1} - \rho_i) r_i^3 / r^2 \right]. \quad (21)$$

The strain tensor is also expressed in terms of the spectral-finite element coefficients  $U_{jm}^{i,k}$ ,  $V_{jm}^{i,k}$  and  $W_{jm}^{i,k}$  (section 7 of Martinec 2000). Because of the assumption of spherical symmetry for the density and elastic structure, the angular dependence in the left-hand side of the variational equality (eq. 16) vanishes after performing the surface and volume integrations. The elastic part of the stress tensor ( $\boldsymbol{\tau}^{E,i+1}$  in eq. 11) can also be represented by the spectral-finite element coefficients as in the strain tensor. On the other hand, the angular dependence of the viscous part of the stress tensor  $\boldsymbol{\tau}^{V,i}$  is numerically evaluated at 2-D latitude–longitude gridpoints. When the viscosity is laterally inhomogeneous, the spheroidal and toroidal coupling occurs in the integration over the angular variable in the dissipation term (eq. 17) at each time step. The integration over longitude is performed by the fast Fourier transform and the integration over latitude is carried out by the Gauss–Legendre quadrature formula (Martinec 2000). The integration over each interval of  $r$  is carried out by means of the two-point Gauss–Legendre numerical quadrature (section 4.5 in Press *et al.* 1992).

The spectral-finite element representation of the source term ( $\delta\mathcal{V}^{i+1}$  in eq. 16) is given in I-(74)–(88). The double-couple forces for a point source are expressed in terms of spherical harmonic expansion coefficients. As in the variations in the left-hand side (eq. 16), the integration over the angular variable can be performed analytically. The resultant forces depend on the location of the source (latitude, longitude and depth), the moment magnitude and the strike, dip and rake angles of the infinitesimal fault. The forces are imposed at the  $k-1$ ,  $k$  and  $k+1$ th layers at each time step. A finite fault is approximated by a set of point sources. For the sake of completeness, the specific representation of  $\delta\mathcal{V}^{i+1}$  for arbitrary focal mechanism is listed in the Appendix A.

## 2.5 The linear algebraic system

The above spectral-finite element representations are substituted into the variational equality (eq. 16). From the condition that the equality holds for all test functions ( $\delta\mathbf{u}$  and  $\delta\phi_1$ ) at each time step, the following linear algebraic equation is finally obtained:

$$\mathbf{A}\mathbf{x}^{i+1} = \mathbf{B}(\mathbf{b}_0^{i+1}, \mathbf{x}^i), \quad (22)$$

where  $\mathbf{x}^{i+1}$  ( $= [U_{jm}^{i+1,k}, V_{jm}^{i+1,k}, W_{jm}^{i+1,k}, F_{jm}^{i+1,k}]$ ,  $k = 1, \dots, P+1$ ) denotes the solution at the current time ( $i+1$ ) and  $\mathbf{A}$  is the time-independent matrix and  $\mathbf{b}_0^{i+1}$  represents the prescribed boundary and source conditions.  $\mathbf{x}^i$  in the right-hand side means that the dissipation term is computed using the solution at the previous time step. Because of the spherical symmetry of the density and elastic structure, the matrix  $\mathbf{A}$  has a band-diagonal form (section 10 in Martinec 2000). The form of  $\mathbf{A}$  is the same as for a surface load in the compressible case with Maxwell rheology. The difference arises only in the right-hand side of eq. (22): the source condition and the time-evolution formula of the viscous part of the stress tensor (eq. 12). The above linear algebraic system is solved by the routines BANMUL and BANBKS based on LU decomposition (Press *et al.* 1992).

## 2.6 Confirmation

### 2.6.1 Test for Maxwell rheology

First, the above formulation is validated with a compressible Maxwell body for which the solution to the same governing equation can be obtained with alternative methods. Considering that the approach is applied to variations in the gravity field, potential changes (or geoid height changes) at the surface are compared. They are represented by  $\phi_1(r=a)$  or  $\phi_1(r=a)/g_0(a)$ . The latter will be compared with satellite observations in Section 3.

As a first step, elastic deformation is confirmed. The analytical solution to an internal dislocation in a spherically symmetric Earth can be obtained by the methods of Gilbert & Backus (1968) and Takeuchi & Saito (1972) or transforming the analytical solution to a surface load (Love 1911; Wu & Peltier 1982) with the reciprocity theorem (Okubo 1993). Here, the latter approach was used. The potential change caused by a point dislocation with an arbitrary fault mechanism can be represented by superimposing the changes caused by three independent fault mechanisms (eq. 78 of Okubo 1993) when the fault normal vector and the slip direction is orthogonal (i.e. the fault opening and a Mogi source are not considered). Table 1 shows the geoid height change caused by a point dislocation buried at a depth of 31 km for spherical harmonic degrees 2, 20, 50 and 100. The density and the elasticity constants  $\mu$  and  $\lambda$  are obtained by averaging those of the PREM (Dziewonski & Anderson 1981) over the five layers above the core–mantle boundary (Table 4). The liquid core is assumed below the core–mantle boundary. The radial intervals between the finite elements,  $\Delta r$ , are also shown in the table. These intervals are almost similar to those used in the incompressible case (table 2 of Tanaka *et al.* 2009). The three independent mechanisms are taken as I: horizontal strike-slip on a vertically aligned fault, II: vertical dip-slip on a vertically aligned fault, and III: dip-slip on an inclined fault with a dip angle

**Table 1.** The fault mechanisms of the point dislocation used for validating the computational method. The last two columns denote the colatitude and longitude of the observation site at which the geoid heights are compared in Table 2. The colatitude and longitude of the source are  $90^\circ$  and  $0^\circ$ , respectively. The depth of the source is 31 km.

Source type	#	Strike	Dip	Rake	$\theta$	$\varphi$
Strike-slip	I	$45^\circ$	$90^\circ$	$0^\circ$	$90^\circ$	$90^\circ$
Dip-slip	II	$0^\circ$	$90^\circ$	$90^\circ$	$30^\circ$	$0^\circ$
Dip-slip	III	$90^\circ$	$45^\circ$	$90^\circ$	$90^\circ$	$0^\circ$

**Table 2.** A comparison between the geoid height changes caused by coseismic deformation of the 6-layer model (Table 3) at the displayed spherical harmonic degrees,  $j$ . The unit is metre and the moment magnitude is normalized using  $UdS = 1 \text{ m}^3$ .

Source type	$j$	Analytic sol.	This study	Per cent diff.
I	2	2.545E-16	2.544E-16	0.03
	20	-5.696E-17	-5.692E-17	0.07
	50	3.790E-17	3.786E-17	0.11
	100	-3.852E-17	-3.847E-17	0.12
II	2	1.915E-17	1.913E-17	0.07
	20	4.356E-17	4.354E-17	0.05
	50	6.833E-17	6.830E-17	0.05
	100	-5.620E-17	-5.617E-17	0.04
III	2	-5.449E-16	-5.451E-16	-0.04
	20	2.919E-16	2.918E-16	0.04
	50	4.476E-16	4.474E-16	0.05
	100	7.104E-16	7.100E-16	0.05

**Table 3.** The earth model parameters used for the confirmation of the elastic response in Table 3.

$r$ (km)	$\Delta r$ (km)	$\rho$ (gcm $^{-3}$ )	$\mu$ (GPa)	$\lambda$ (GPa)
0–3481	10	10.99	0	–
3481–5701	5	4.88	219	344
5701–5971	5	3.86	106	146
5971–6151	5	3.48	76.5	111
6151–6311	5	3.37	66.8	77.0
6311–6371	1	3.03	52.5	62.6

of 45°. The specific strike, dip and rake angles and the positions of observation sites at which the computed results are compared with the analytical solutions are shown in the table. The relative difference from the analytical solution is less than approximately 0.1 per cent. Compared with a similar comparison in the load Love numbers (Tanaka *et al.* 2011), however, these differences are 3–12 times larger. This might be due to the fact that the source term is more complicated in the dislocation problem. In the case of surface loading, a single vertical force is applied to the surface layer and only the spheroidal motion is excited. In contrast, the source term

**Table 4.** Fault model parameters determined by inversion of the GRACE data. The geometry of the faults is described in Banerjee *et al.* (2007). The asterisks attached to the numbers denote the fault planes extended downwards to infer afterslip.

#	This study		Banerjee <i>et al.</i> (2007)		
	Rake (°)	Slip (m)	ID	Rake (°)	Slip (m)
1	88	6.3	1E	139	6.6
2*	82	4.2	1A	139	0
3	84	6.7	1F	139	5.2
4*	74	5.0	1B	122	0
5	85	7.3	1G	115	7.8
6*	79	5.2	1C	115	0
7*	80	5.4	1D	105	2.3
8	86	7.9	1H	105	16.6
9*	123	0.9	2A	0	0
10	97	12.6	2B	110	19.4
11	96	5.8	2C	0	0
12*	95	5.6	3A	90	15.5
13*	113	5.5	3B	90	0.5
14	94	9.6	3C	90	15.5
15	104	8.9	3D	90	9.2
$\sum UdS$ (m $^3$ )		$1.8 \times 10^{12}$			$1.5 \times 10^{12}$

for a dislocation consists of more than one force, having different directions, and they are applied to different depths. As a result, both spheroidal and toroidal motions occur. A typical coseismic gravity change generated by a great earthquake is 1–10  $\mu\text{Gal}$  at wavelengths of  $\sim 400$  km when observed by the GRACE (fig. 3 in Matsuo & Heki 2011). Considering that the uncertainties of temporal variations in the gravity field derived from the GRACE data amount to 1–2  $\mu\text{Gal}$  (Section 3) and the advantage that the method enables us to consider the effects of compressibility that exceed 10 per cent (Tanaka *et al.* 2006; Cambiotti *et al.* 2011) and 3-D viscosity distributions, the price of the above error in the theoretical estimate would be practically acceptable for general modelling.

Next, the viscoelastic deformation is analysed using the method of Tanaka *et al.* (2007). This method uses a numerical inverse Laplace integration to obtain a post-seismic viscoelastic response of a spherically symmetric earth model. As a practical example, the geoid height change caused by the 2004 Sumatra–Andaman earthquake is estimated. As an initial value for calculating viscoelastic relaxation, the coseismic slip distribution of Chlieh *et al.* (2007) is adopted. The rectangular fault planes are approximated by 200 point sources on which the rake angles and slip amounts vary in space. The locations of the sources are drawn by small open circles in Fig. 1 ( $t = 0$ ). As an earth model, PREM with an elastic lithosphere of thickness of 50 km is employed. Below the lithosphere, the viscosity is  $10^{19}$  Pa s throughout the mantle, which is assumed to be Maxwell viscoelastic. The number of the layers is approximately 1000, and the density and elastic parameters at each layer is determined, using the interpolation equations in PREM. In the finite-element computation, the radial intervals are the same as before. The time step in the computation of the time evolution is 0.1 yr. Fig. 1 shows the result obtained by the spectral-finite element approach. Here,  $t = 25 - t = 0$  denotes the deformation at  $t = 25$  (yr) minus the instantaneous elastic change. The cut-off degree is 100, and only the deformation of the solid Earth is considered. No spatial filter is applied to the result. It can be observed that the geoid height increases at  $t = 0$  and decreases after  $t = 0$  near the source area at this cut-off degree. As will be demonstrated in Section 3, when the cut-off degree is decreased to 50 and the effects from the ocean mass redistribution by the ocean bottom deformation are added, the sense of the dominant change becomes opposite. Fig. 2 shows the profiles of the geoid height change on dotted lines A and B in Fig. 1. The result from the alternative method (Tanaka *et al.* 2007) is superimposed. The comparison method has relative uncertainties of a few per cent (Tanaka *et al.* 2007). Relative errors due to the finite-element approximation in the presented method can be estimated by comparing the computed results for smaller discretisation intervals for the radial coordinate. When reducing the sizes described in the above by one-half, the largest differences on line A become 0.07 mm at  $t = 0$  and 0.15 mm at  $t = 50$  yr. Considering the computational errors in both methods, the results in Fig. 2 appear to agree with one another within the errors. The above result indicates that the spectral-finite element representation is correct for the special case of  $\eta_2 = \infty$ .

### 2.6.2 Test for Burgers rheology

In the case of a Burgers body, the solution to the identical governing equations for a spherical earth model has not yet obtained. Therefore, the representation of the time evolution formula is self-checked using the spectral finite-element method, using a 1-D (i.e. spherically symmetric) model. In Section 2.4, it was mentioned

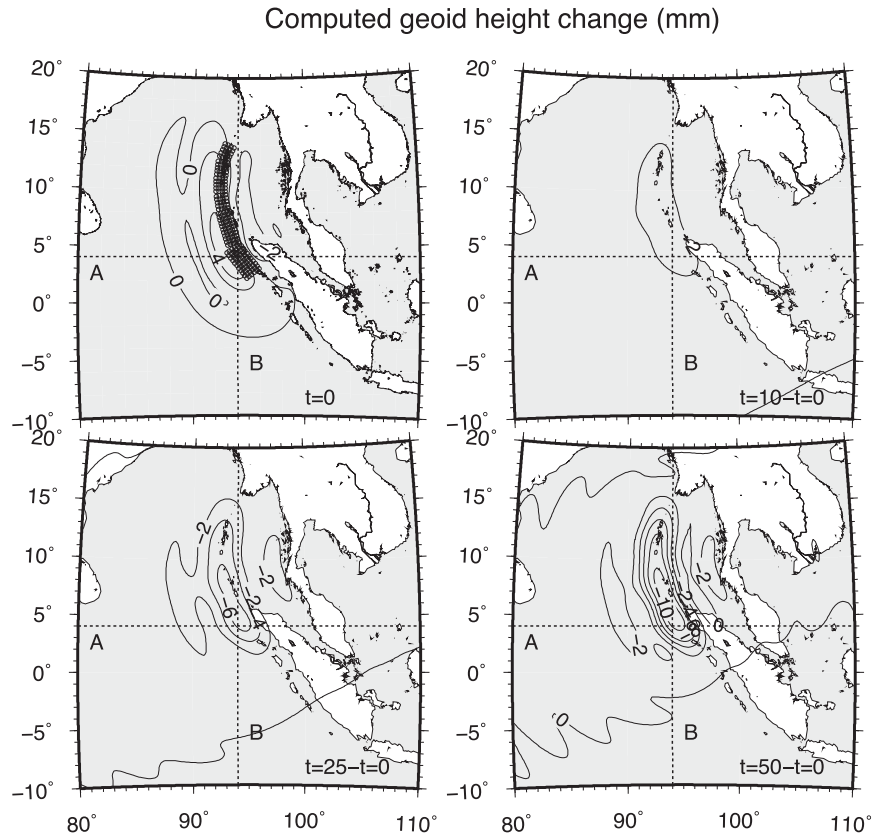


**Figure 1.** Co- and postseismic geoid height changes due to the 2004 Sumatra event, obtained by the developed method at different time steps, 0, 10, 25 and 50 yr after the event. The contour interval is 2 mm. The viscoelastic relaxation of the solid Earth with Maxwell rheology is considered. The earth model is described in the text. The cut-off degree is 100. The profiles on dotted lines A and B are discussed in Fig. 2.

that the dissipation term is evaluated by a numerical volume integration. However, when the viscosity structure is 1-D, the integration over the angular variable can be performed analytically, using the orthogonality of the tensor spherical harmonics. For this reason, an alternative finite-element representation can be used in the 1-D case (see Sections 8 and 9 of Martinec 2000, for the details). By comparing the result obtained using the 3-D routine with that obtained using the 1-D routine, the correctness of both representations can be tested. In the gravity change patterns presented in Section 3 (Figs 9c, d and 12), the agreement is within at least 1 per cent in the gravity field changes. Relative errors in the finite-element calculation can also be estimated, as in the above-mentioned case of Maxwell material. The reference values of  $\Delta r$  are the same as before. The largest differences in gravity change that appear when decreasing  $\Delta r$  by one-half are  $0.04 \mu\text{Gal}$  at  $t = 0$  and  $0.26 \mu\text{Gal}$  at  $t = 6.5$  yr above the source area. These values are less than the observational noises of the GRACE.

From the above confirmations, the developed method is considered to have sufficient computational accuracy for practical use.

### 3 APPLICATION

#### 3.1 An overview

Post-seismic gravity field variations caused by the 2004 Sumatra–Andaman Earthquake have been studied by several researchers as mentioned in Section 1. However, in most studies, coseismic fault models are determined by the GNSS and seismological observations (e.g. de Linage *et al.* 2009; Panet *et al.* 2010), which indicate

that different observation techniques other than satellite gravity are combined to study post-seismic deformation mechanisms. A coseismic slip distribution model serves as the initial value for computing viscoelastic relaxation. This viscoelastic effect is subtracted from the observed data, and afterslip is inferred against the remaining signal. Therefore, the adopted coseismic fault model affects the estimates of both viscoelastic relaxation and afterslip. In this study, to exclude the possibility that combining data obtained by different observation techniques can produce differences in the inferred mechanisms, only GRACE data are analysed. A coseismic fault model is re-evaluated by inverting GRACE data. Post-seismic deformation mechanisms are investigated in this section by comparing observed spatial patterns in the gravity field with theoretically predicted patterns of afterslip, viscoelastic relaxation, poroelastic rebound and so on. Moreover, the effects of the laterally heterogeneous viscosity structure due to the presence of a slab on viscoelastic relaxation are presented. Differences between the results obtained in this study and those derived from previous studies are discussed in Section 4.

#### 3.2 GRACE data

To extract space–time variations in the gravity field associated with co- and post-seismic deformations, GRACE Level-2 products are analysed, using a method that is similar to Hasegawa *et al.* (2009). The Level-2 data are provided by different data analysis centres in the form of monthly Stokes' coefficients. In this study, results from the CSR and the GFZ are employed. The raw data are corrected for the effects of continental water and ocean circulation with the Global Land Data Assimilation System (GLDAS)

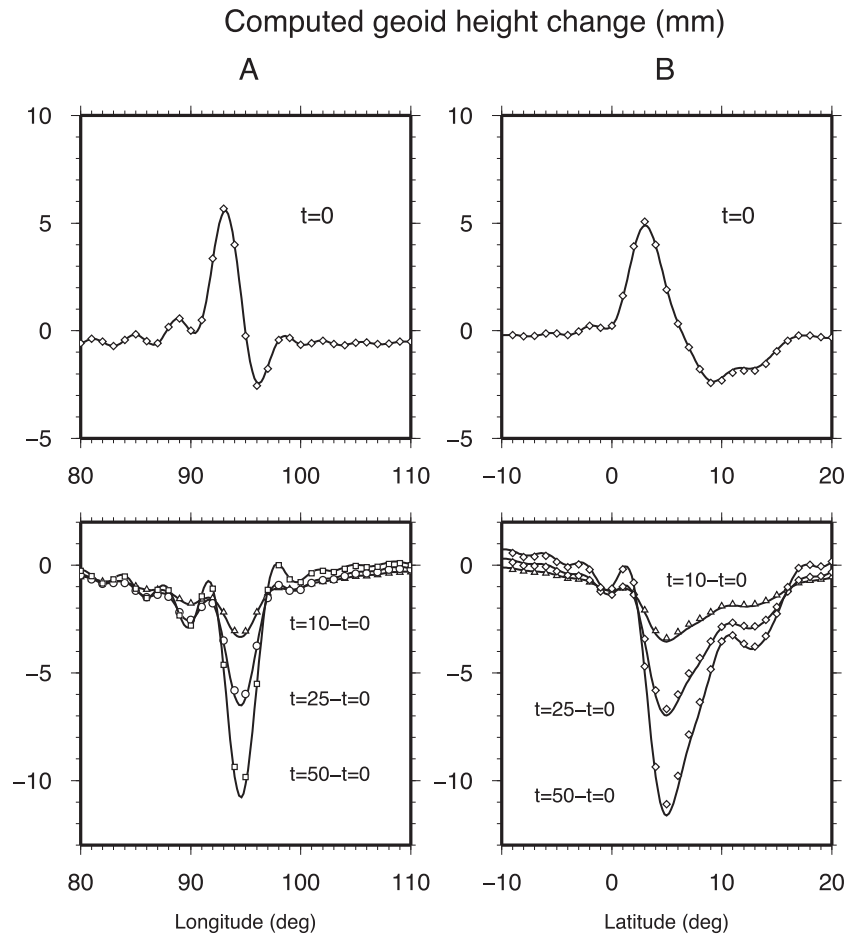


**Figure 2.** The geoid height change on line A (left-hand side) and B (right-hand side) in Fig. 1. The vertical axis is presented in mm units, and the horizontal axis indicates longitude or latitude. Co- and post-seismic changes are plotted on the upper and the lower panels, respectively. The solid line shows the result obtained by the method presented in this study, and the squares display the result computed by the numerical Laplace integration method for the same model.

and Estimating the Circulation and Climate of the Ocean (ECCO) models, respectively. These models are available at the NASA website: <http://disc.sci.gsfc.nasa.gov/services/grads-gds/gldas> and <http://ecco.jpl.nasa.gov/datasets/kf080/>. To determine the effects of using different correction models for continental water, results obtained using the Community Land Model (CLM; Dai *et al.* 2003) and the Noah model (Chen *et al.* 1996; Koren *et al.* 1999) are compared (i.e. four gravity fields are obtained per month: CSR–CLM, CSR–NOAA, GFZ–CLM and GFZ–NOAA). Artificial stripping noises that appear in the N–S direction in the resultant gravity variations are decorrelated and filtered using the method of Swenson & Wahr (2006) and the Jekeli’s Gaussian averaging function (Jekeli 1981), respectively. The radius for the latter is set to 400 km, and the cut-off degree is set to 50.

### 3.3 Observed gravity change patterns

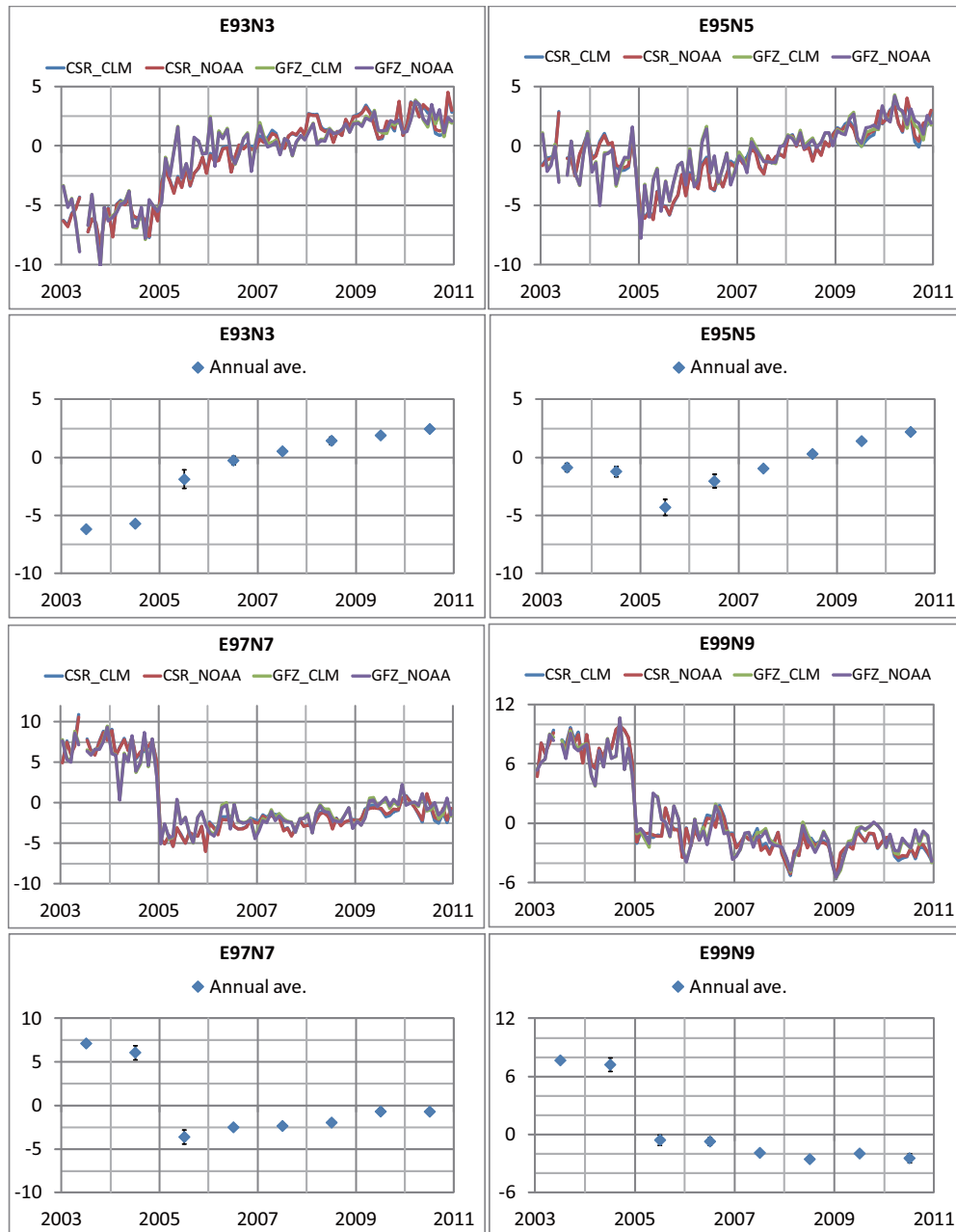
#### 3.3.1 Coseismic change

Fig. 3 shows the observed time-series for gravity changes during the 2003–2011 period at four sites near the epicentre. The results for the four combinations of the gravity fields are plotted by the colour lines. The differences between the hydrological models at these sites are smaller than  $1 \mu\text{Gal}$  throughout the whole observation period and the underlaid blue (CSR–CLM) and green (GFZ–CLM) lines almost cannot be distinguished from the respective NOAA curves.

The differences caused by the products of the different analysis centres are larger ( $1\text{--}3 \mu\text{Gal}$ ). However, the longer-term (greater than 1 yr) trends closely agree with one another. When averaging the annual average values for the four cases, the standard deviations become less than  $1 \mu\text{Gal}$  (Fig. 3).

The coseismic change due to the Sumatra earthquake can be estimated by subtracting a reference gravity field before the event from the gravity field after the event. Considering deviations in the monthly gravity changes in a single year shown in Fig. 3 ( $\pm 1\text{--}3 \mu\text{Gal}$ ), subtracting the result of 2004 December from that of 2005 January is less accurate. In general, hydrological and oceanic effects are dominated by seasonal variations. The time-series plots of the monthly data indicate that the patterns of annual variations differ according to the observation sites. Particularly, the annual variations at E99N9 are the most remarkable. To cancel out such variations depending on geographical location, the reference gravity field before the event is calculated by averaging the monthly data over 12 months during the year 2004. The post-event gravity fields are computed by averaging the monthly data during the following two periods: (A) from 2005 January to 2005 March (3 months) and (B) from 2005 January to 2005 December (12 months).

The gravity change obtained by subtracting the reference gravity field from those for the period A is shown in Fig. 4 and from those for the period B is shown in Fig. 5. The plots in Figs 4(a–c) present the result of combinations of CSR–NOAA, GFZ–NOAA and GFZ–CLM. The spatial changes in any of these are characterized



**Figure 3.** Time-series plots of the gravity changes at four sites derived from the GRACE data analysis. E93N3, etc. means longitude 93°E and latitude 3°N. The unit on the vertical axis is the  $\mu\text{Gal}$ . The coloured lines superimposed on one another denote the gravity changes from the different GRACE data analysis centres (CSR/GFZ) and the different hydrological correction models (CLM/NOAA). The figures with blue data points below these plots represent the annual average of the mean of all four ( $=2 \times 2$ ) time-series data sets. The 2004 Sumatra–Andaman earthquake occurred on 2004 December 26.

by the larger negative anomaly to the northeast and the smaller positive anomaly to the southwest of the source area. As observed in the time-series data (Fig. 3), the patterns of (b) and (c) agree with one another within  $1 \mu\text{Gal}$ , indicating that the differences in the hydrological models are minor. The difference between the analysis centres are larger, and the peak value of the negative anomaly is  $2 \mu\text{Gal}$  lower in (a) than in (b). The peak location of the positive anomaly to the southwest is also shifted to the south in (a) compared with the case in (b) by approximately  $2^\circ$ . These plots demonstrate that the analysed gravity changes obtained using the 3-month post-event data have uncertainties of  $1\text{--}2 \mu\text{Gal}$ . Figs. 5(a–c) present the results obtained using the data during period B. The same feature as

in Fig. 4 is observed during the period from 2004.5 to 2005.5. The plots (d) of the two figures show the average calculated by all four combinations of the gravity fields obtained using the post-event data during periods A and B, respectively. Comparing Figs 4(d) and 5(d), the longer-wavelength variations on the ocean and on the continent become smaller, and the variations due to the earthquake appear to be more emphasized in Fig. 5(d). However, the spatial patterns of Figs 4(d) and 5(d) are substantially similar, and the difference is only approximately  $1 \mu\text{Gal}$ . During the period between A and B (i.e. 2005.125–2005.5), the post-seismic deformation should cause gravity variation. However, uncertainties stemming from the deviations observed between Figs 4(a–c) and Figs 5(a–c) make it

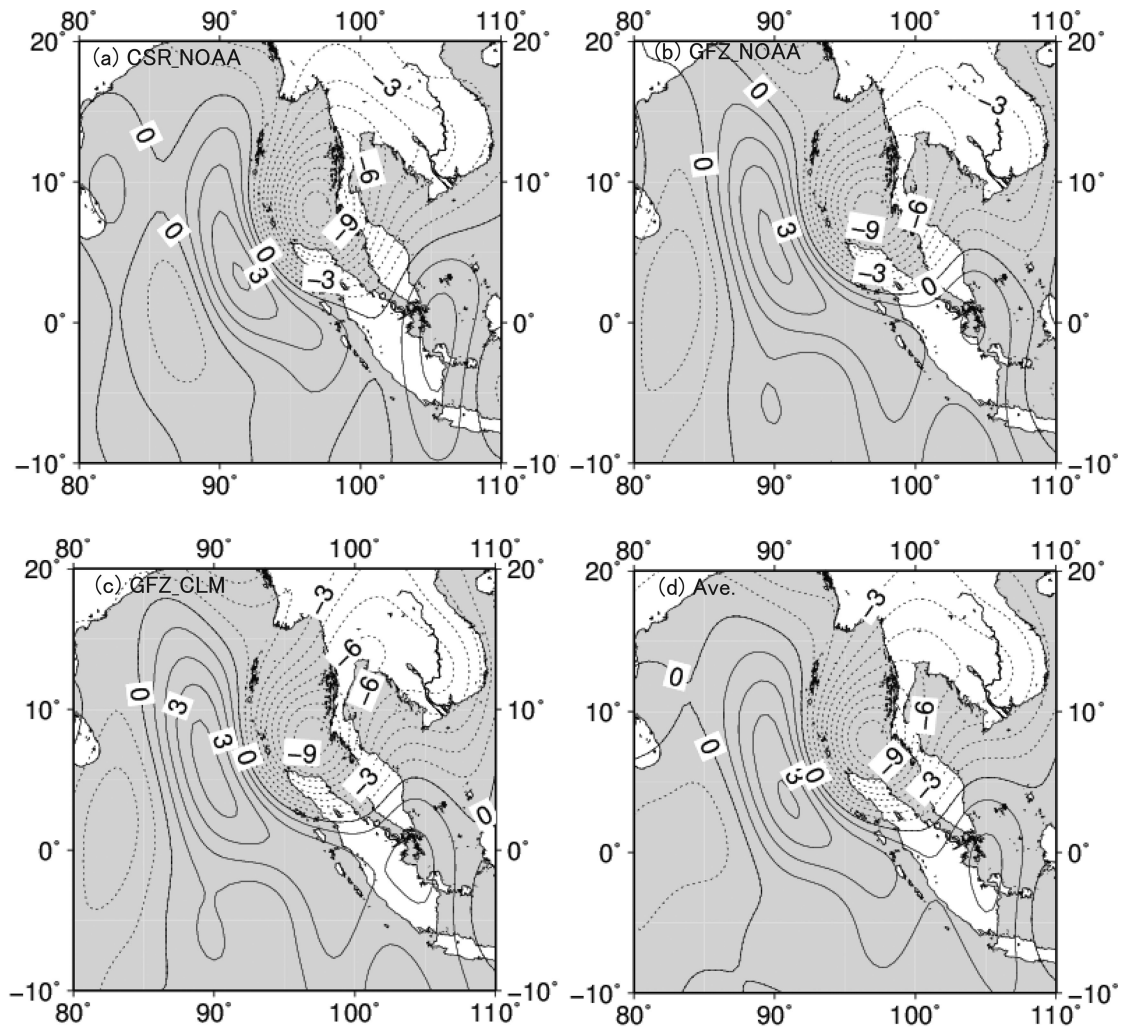


**Figure 4.** The observed gravity change patterns obtained by subtracting the average of the 12-month data during 2004 from the average of the 3 months from January to March in 2005. The units are  $\mu\text{Gal}$ , the contour interval is  $1 \mu\text{Gal}$  and dotted lines denote negative changes. Panels (a), (b) and (c) represent the difference in the GRACE data analysis centres (CSR/GFZ) and the hydrological models (NOAA/CLM). Panel (d) is the mean of the four data sets (CSR–NOAA, CSR–CLM, GFZ–NOAA and GFZ–CLM).

difficult to discern the post-seismic signal. In the following discussion, the annual average values of the mean of the four data sets are used to improve precisions of the observed gravity changes, which means that the substantial temporal resolution of the observed gravity changes becomes longer than 1 month. In Fig. 3, time-series plots of the annual averages of the four combinations are shown in panels below the respective time-series. It follows that the coseismic change is included in the difference that arose between 2004.5 and 2005.5. The change during this period is clearly larger than the uncertainties (the error bars indicate standard deviations between the four combinations and are often masked by the diamond icon).

### 3.3.2 Post-seismic change

From the time-series plots in Fig. 3, a transient gravity change signal can be identified during the 2005–2011 period. Fig. 6 shows the spatial patterns of the transient changes during the presented four periods after 2005.5. In Figs 6(a–d), the single positive anomaly is commonly observed at the source area. The total change cumulates to  $7 \mu\text{Gal}$  during 6 yr (Fig. 6a), and approximately one-half of

this change occurred until 2008.5 (Fig. 6b). The spatial patterns in Figs 6(a–d) differ significantly from the patterns in Figs 4(d) and 5(d). It is noted that the centres of the positive anomalies in Figs 6(a–d) are shifted northeast in comparison to those in Figs 4(d) and 5(d). As will be demonstrated further down, the spatial patterns observed after 2005.5 closely agree with the spatial pattern of a theoretically predicted viscoelastic relaxation.

## 3.4 Theoretical interpretations of the observed results

### 3.4.1 Coseismic change

First, the coseismic gravity change is estimated by applying fault models determined by other observation techniques as from previous studies. Figs 7(a) and (b) show the results computed by the method presented in Section 2 with the fault models of Ammon *et al.* (2005) and Banerjee *et al.* (2007). The former and the latter are used in de Linage *et al.* (2009) and Panet *et al.* (2010), respectively, for estimating gravity changes. For the latter, the fault parameters of model C in table 2 of Banerjee *et al.* (2007) are employed. The

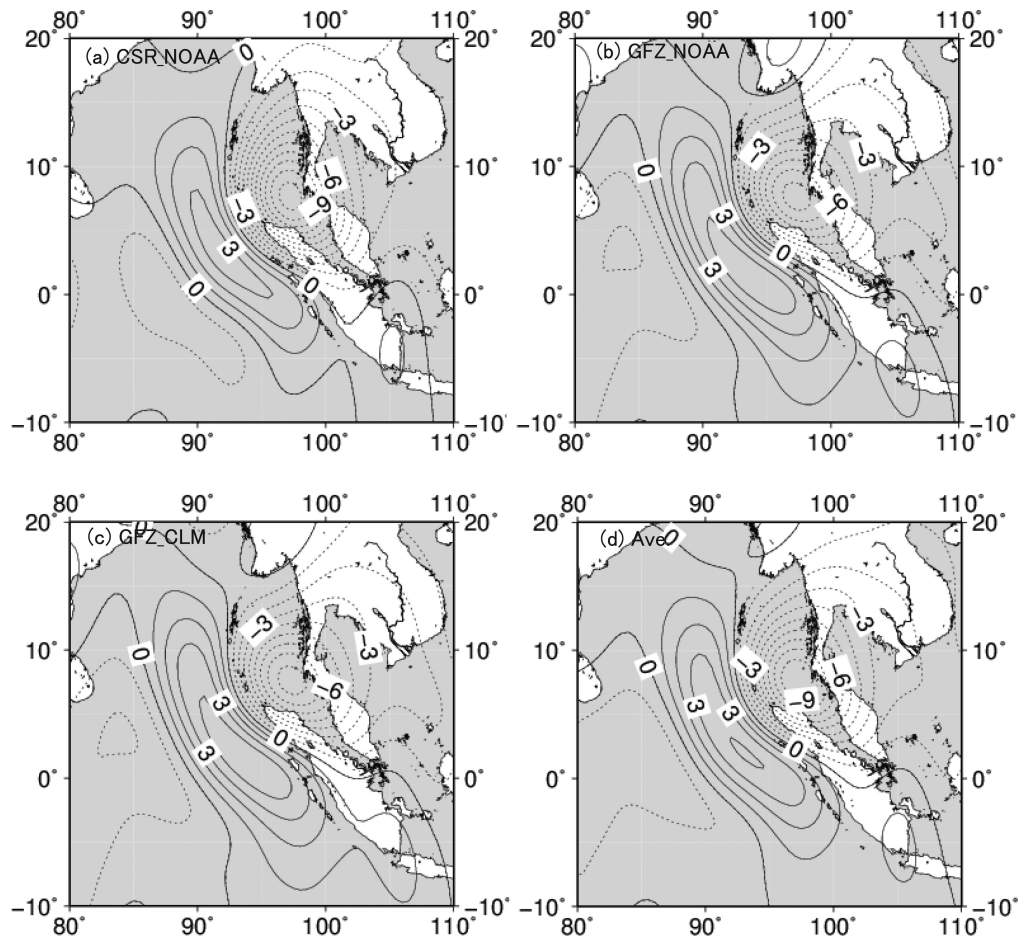


**Figure 5.** The observed gravity change patterns like in Fig. 4, but the post-event gravity fields are calculated by averaging the 12-month data during 2005.

density and the elastic structures are those of PREM. In addition to the gravity change due to the deformation of the solid Earth, a redistribution of ocean mass caused by the vertical deformation of the ocean bottom is considered. The necessity of correcting the effect due to the ocean mass redistribution is stated, for example in de Linage *et al.* (2009) and Broerse *et al.* (2011). The effect of the horizontal deformation of the ocean bottom is more than one order of magnitude smaller than the effect of the vertical deformation (Appendix B) and is neglected in the following discussion. The cut-off degree and the radius of the filter are the same as for the GRACE data (50 and 400 km). The spatial patterns predicted by the theory for both fault models appear to reproduce the observed pattern in Fig. 5(d). However, these estimates consider only the effects of coseismic change. Banerjee *et al.* (2007) presents a fault model of afterslip during the first 50 d after the main event and that of the coseismic slip for the 2005 March 28 Nias Earthquake (Appendix C). Fig. 7(c) shows the sum of the coseismic gravity change due to the main event (Fig. 7 b) and the gravity changes caused by these two processes. Comparing Figs 7(b) and (c), both the negative and the positive anomalies are enhanced by approximately  $1 \mu\text{Gal}$ . Fig. 7(c) appears to explain the observed pattern better. However, when subtracting the pattern shown in Fig. 7(c) from the observed pattern shown in Fig. 5(d), the result is shown in Fig. 7(d), a systematic difference appears near the source area with an amplitude larger than the uncertainties of the annual average values ( $<1 \mu\text{Gal}$ ). A similar negative change exceeding the observational errors is also observed for the case with the fault model of Ammon *et al.* (2005, figure not shown).

Assuming that the fault model inferred from GPS data (Banerjee *et al.* 2007) is accurate, this systematic pattern should be reproduced by the post-seismic deformations that occurred until 2005.5. Fig. 8 shows the gravity-change patterns predicted by afterslip, splay fault and poroelastic rebound. Fig. 8(a) represents the change expected from afterslip during the first 0.5 yr. It is assumed that during the first 50 d the afterslip distribution on the fault planes which extend downward from the coseismic rupture zone (Banerjee *et al.* 2007) remains the same and that the temporal evolution of the slip follows  $\log(t)$  (Marone *et al.* 1991; Hashimoto *et al.* 2006). In other words, Fig. 8(a) can be obtained by multiplying a factor of  $\log 0.5 \text{ yr} \log 50 \text{ d}^{-1}$  to the gravity change calculated for the afterslip model of Banerjee *et al.* (2007). This pattern is positive at the source area and, therefore, cannot explain the large negative anomaly visible in Fig. 7(d). Fig. 8(b) shows the coseismic change due to a splay fault near the surface. This fault model is constrained by geodetic data (Banerjee *et al.* 2007) and the inferred pattern does not agree with that in Fig. 7(d), either. Hughes *et al.* (2010) reported that the 2005 Nias earthquake could be triggered by poroelastic deformation due to the 2004 event. Fig. 7(c) shows the gravity change caused by a hypothetical large-scale poroelastic rebound that occurs within the whole crust of 50 km thickness. If poroelastic rebound is limited only near to the surface, the gravity change that exceeds  $1 \mu\text{Gal}$  cannot be reproduced. The gravity change by the poroelastic rebound is computed by considering only the initial and equilibrium states. For the calculation of the instantaneous response at the initial state, a modified PREM is assumed where the Poisson's ratio within the crust is decreased by 0.05. For the equilibrium state, the original

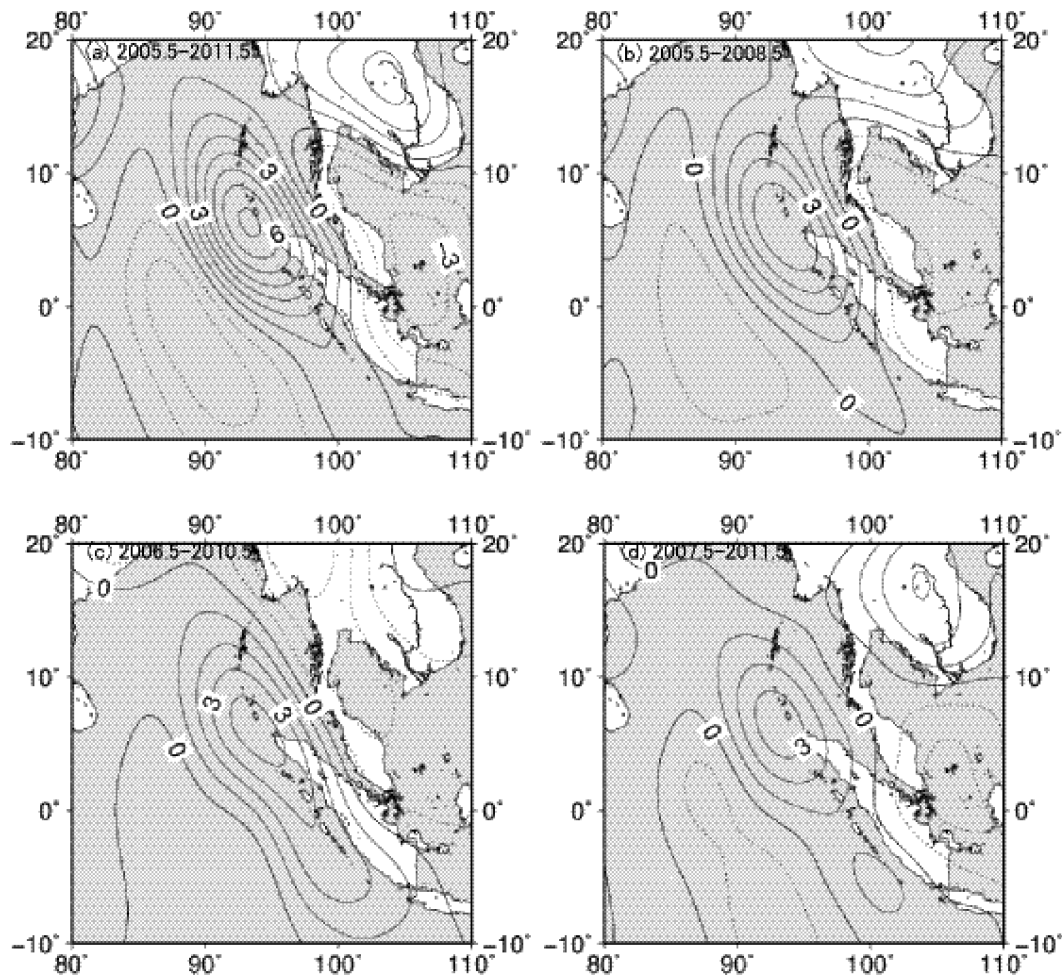


**Figure 6.** The post-seismic gravity change patterns obtained from the annual averages of the mean of the four data sets. The changes that occurred during the 2005.5–2011.5, 2005.5–2008.5, 2006.5–2010.5 and 2007.5–2011.5 periods are drawn in (a)–(d), respectively. The units are  $\mu\text{Gal}$ , the contour interval is  $1 \mu\text{Gal}$  and dotted lines denote negative changes.

PREM is applied. The resulting change is positive above the source area. By way of experiment, a poroelastic rebound in the mantle can be considered. Fig. 7(d) shows the result for the case in which Poisson's ratio for the depth range from 50 to 350 km is decreased by 0.1 at the initial state. Only by this hypothetical poroelastic rebound mechanism, a pattern similar to the observed negative anomaly can be generated. Independent observations supporting this mechanism have not been found. From the above consideration, there is some evidence that the fault models determined by the GNSS and the seismic observations are not necessarily consistent with the GRACE observations. Inconsistency between the results from the GNSS and seismic observations has also been reported (Ammon *et al.* 2005).

### 3.4.2 Coseismic slip distribution inferred from GRACE data

The above result implies that the fault model can be improved by incorporating GRACE data into the analyses of the ground deformation data. In this study, as a first step, only GRACE data are employed. The slips and their directions on the 15 rectangular fault planes in table 1 of Banerjee *et al.* (2007) are redetermined by the least-squares method. The 15 rectangular faults are approximated by 540 point sources in total. Green's functions of the dip and

strike components of slip are computed for each point source by the presented method and the other parameters (such as the strike and dip angles of the faults) are fixed. Because parameters are the same on each rectangular fault, no smoothing and constraints are applied to the slip inversion. The observed gravity change until 2005.5 (Fig. 5d) is discretized on a  $2^\circ \times 2^\circ$  grid in the range from  $85^\circ\text{E}$  to  $105^\circ\text{E}$  and from  $-5^\circ\text{N}$  to  $10^\circ\text{N}$  is used for the inversion (i.e. 121 observation sites). Note that the fault planes include extended portions from the coseismic rupture zones, which indicates that the sum of the coseismic slip and afterslip until 2005.5 is inferred.

Table 4 shows the inferred fault parameters. A significant difference from the coseismic slip distribution of Banerjee *et al.* (2007) is that the slips on the additional faults, which are used to explain afterslip, have non-zero values due to an observation-period expansion of approximately 0.5 yr. The sum of the products of the slip and area for the 15 faults,  $\sum U dS$ , shown in the last line of Table 4, increased from  $1.5 \times 10^{12}$  to  $1.8 \times 10^{12} \text{ m}^3$ . The increase in  $\sum U dS$  corresponds to a moment magnitude of 8.6 when the rigidity of the crust,  $\mu_c = 30 \text{ GPa}$ . The obtained rake angles for subfaults numbers 1–8 are  $74^\circ$ – $88^\circ$ , and, so, by approximately  $20^\circ$ – $30^\circ$  smaller than those of Banerjee *et al.* (2007). The rake angles in Banerjee *et al.* (2007) agree with background plate motions and the seismically derived slip models, and their uncertainties are  $5^\circ$ – $8^\circ$  (Banerjee *et al.* 2005). In our inversion, the sensitivity for the rake angles is very

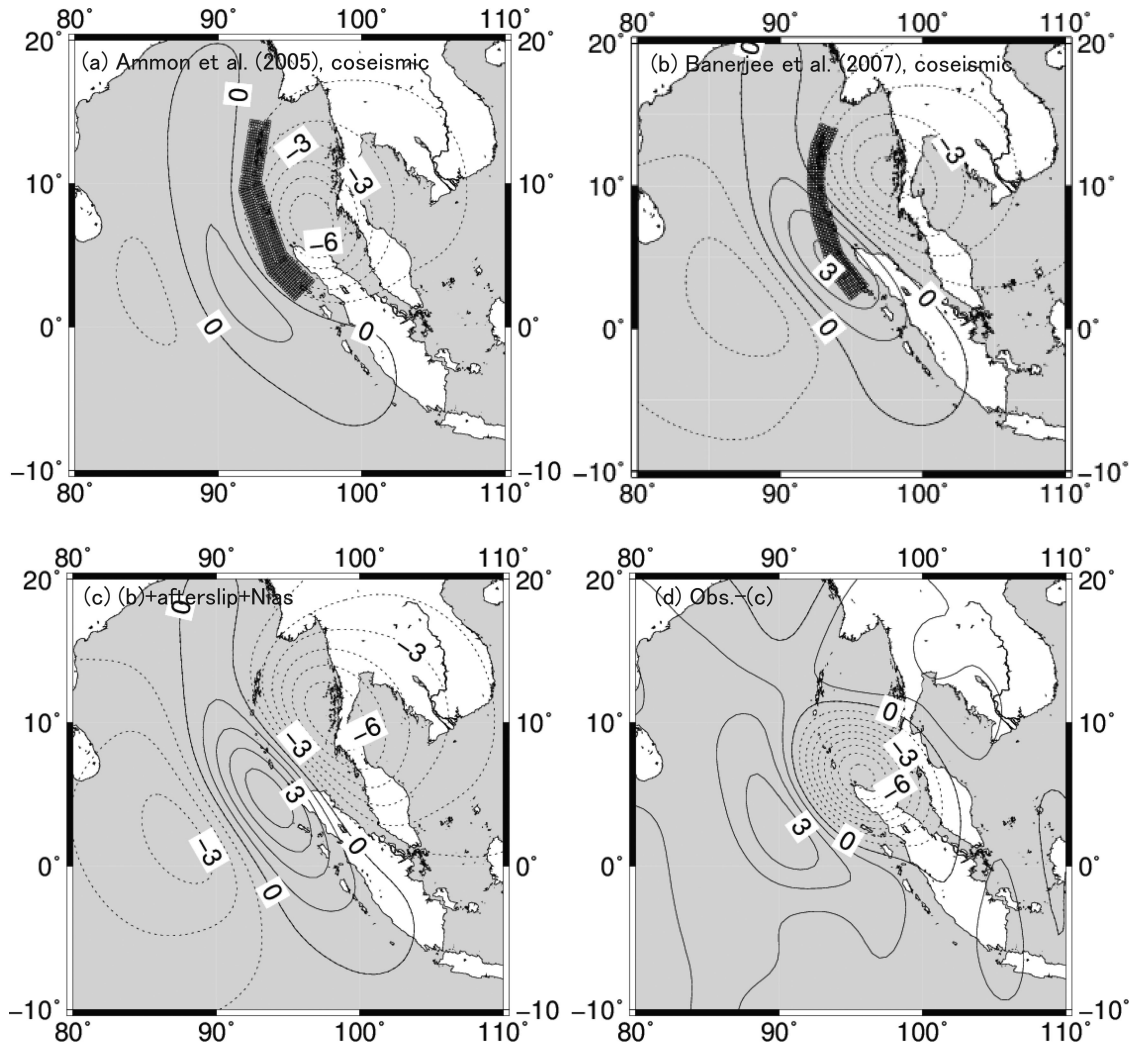


**Figure 7.** (a and b) The gravity changes caused by the instantaneous elastic response due to the 2004 Sumatra event. The fault models of Ammon *et al.* (2005) and Banerjee *et al.* (2007) are employed in (a) and (b), respectively. The units are  $\mu\text{Gal}$ , the contour interval is 1  $\mu\text{Gal}$  and dotted lines denote negative changes. The point sources to approximate the fault segments are represented by sets of small black circles. (c) The sum of the coseismic change in (b), the effect of afterslip during the first 50 d, and the contribution from the coseismic change by the 2005 Nias event (Fig. C1). (d) The observed pattern in Fig. 5(d) minus the pattern in Fig. 7(c).

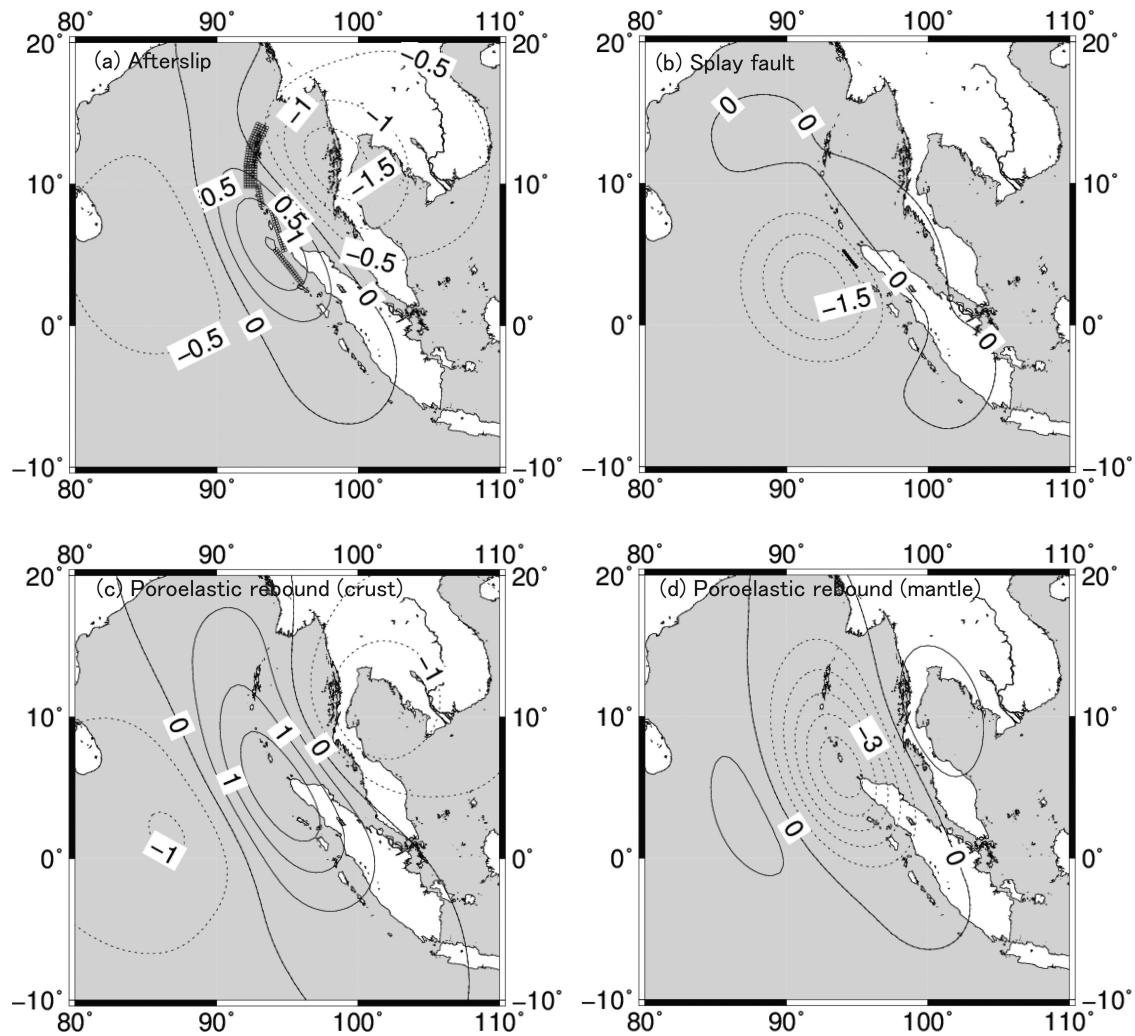
low. A change in rms by only 0.01  $\mu\text{Gal}$  would allow to increase the rake angles of all subfaults. Furthermore, the differences in the rake angles from those in Banerjee *et al.* (2007) become larger with distance northward along the rupture. The horizontal displacement at 94°E and 14°N can be computed using the method of Tanaka *et al.* (2007). The NS and EW components are (−0.30 m, −0.83 m) when our slip model is employed and (+0.14 m, −1.47 m) when the rake angles are increased by 20°. The difference in the displacements is large enough to be detected by GPS. This means that the coseismic slip distribution determined only by GRACE is still inconsistent with the result determined by GPS. Cambiotti *et al.* (2011) explained the coseismic gravity change computed from GRACE data by changing the depths and the dip angles of a seismic source model (Tsai *et al.* 2005), implying a further inconsistency between the GRACE and seismic data.

Fig. 9(a) shows the gravity change computed by the inferred fault model, indicating that the negative anomaly in the observation (Fig. 5d) is well reproduced. However, the positive anomaly observed to the southwest disappears. Subtracting the patterns in Fig. 9(a) and the coseismic change by the Nias event (Fig. C1)

from the observed pattern (Fig. 5d), a positive gravity change of approximately 6  $\mu\text{Gal}$  is observed over the source area (Fig. 9b). The afterslip pattern (Fig. 8a) cannot explain this positive anomaly because an increasing afterslip will generate a larger negative change to the northeast than a positive change just above the source area. Fig. 8(a) indicates that the amplitude of the negative change is approximately 1.5 times larger than the positive one.

### 3.4.3 Post-seismic relaxation

The remaining positive anomaly until 2005.5 (Fig. 9b) appears to be similar to the transient gravity change patterns observed after 2005.5 (Figs 6a–d). The change before 2005.5 may also be explained by the same mechanism as for the change after 2005.5. In the following discussion, it is shown that the positive changes observed during the whole observation period can be interpreted by viscoelastic relaxation with Burgers rheology. An alternative interpretation of the change before 2005.5 is that this change was caused by diffusion of mantle water immediately after the Sumatra event (Ogawa & Heki 2007).



**Figure 8.** The gravity change patterns predicted by possible mechanisms. Panel (a) afterslip, (b) slip on a splay fault, (c and d) hypothetical poroelastic rebounds within the crust and in the mantle, respectively. In panels (a) and (b), the positions of the point sources to approximate the faults are shown by sets of small black circles. The units are  $\mu\text{Gal}$ , the contour interval is  $0.5 \mu\text{Gal}$  and dotted lines denote negative changes.

Viscoelastic relaxation by the coseismic slip and the afterslip of the main event can be estimated using the fault model determined by the inversion (see Fig. 9a and Table 4). The temporal evolution of the afterslip is neglected, and it is assumed that the afterslip occurred simultaneously with the coseismic slip. A contribution from the coseismic slip of the Nias event and its viscoelastic relaxation is computed using the fault model of Banerjee *et al.* (2007). Because the temporal resolution of the observation data is 1 yr, this contribution is added at and after 2005.5, although it occurred before 2005.5. Afterslip of the Nias event is neglected here as it would be smaller than the coseismic gravity change of  $1 \mu\text{Gal}$ , which cannot be discerned by GRACE. The elasticity and density structure is that of PREM. The viscosity distribution is also assumed to be spherically symmetric. The thickness of the elastic lithosphere is set to 70 km. A similar value of the lithosphere thickness (60 km) is used in Panet *et al.* (2010) for explaining the post-seismic GRACE geoid change. Burgers rheology is assumed from a depth of 70 to 300 km. Below 300 km, the viscosity is set to  $10^{21}$  Pa s. In the unlikely case, that the viscosity below 300 km is as low as the viscosity in the overlying layer, the computed positive anomaly above the source becomes broader, and the surrounding zero contour line moves outside by approximately 1000 km. This is in contrast to the observed pattern

(Fig. 6a) indicating the area with positive change to be bounded from  $90^\circ\text{E}$  to  $100^\circ\text{E}$ . In the viscoelastic layer,  $\mu_1 = \mu_2$  is assumed to reduce the number of parameters (eq. 7). The viscosities,  $\eta_{1,2}$ , are determined by trial and error so that the maximum of the positive anomaly in the predicted gravity change during the periods before 2005.5 and from 2005.5 to 2011.5 become as close as possible to the observed ones, Fig. 9(b) and Fig. 6(a), respectively. To be exact, the coseismic change from the Nias event in Fig. 9(b) must be added back. However, its effect is small and almost negligible in the determination of the parameters. Using this method,  $\eta_1 = 6 \times 10^{18}$  Pa s and  $\eta_2 = 6 \times 10^{17}$  Pa s were obtained.

Figs 9(c) and (d) show the gravity changes caused by viscoelastic relaxation during both periods. There is good agreement between the patterns of Figs 9(b) and (c) and those of Figs 6(a) and 9(d). When adopting Maxwell rheology, the longer-term change can be explained with viscosity values of the order of  $10^{18}$  Pa s. However, an additional mechanism for the short-term positive anomaly is required, as stated in Ogawa & Heki (2007). Fig. 10(a) shows the gravity change at 2005.5, calculated with the above-mentioned model based on Burgers rheology. By adding the short-term relaxation, the positive anomaly in Fig. 9(b) is reproduced; consequently from Fig. 10(a), it

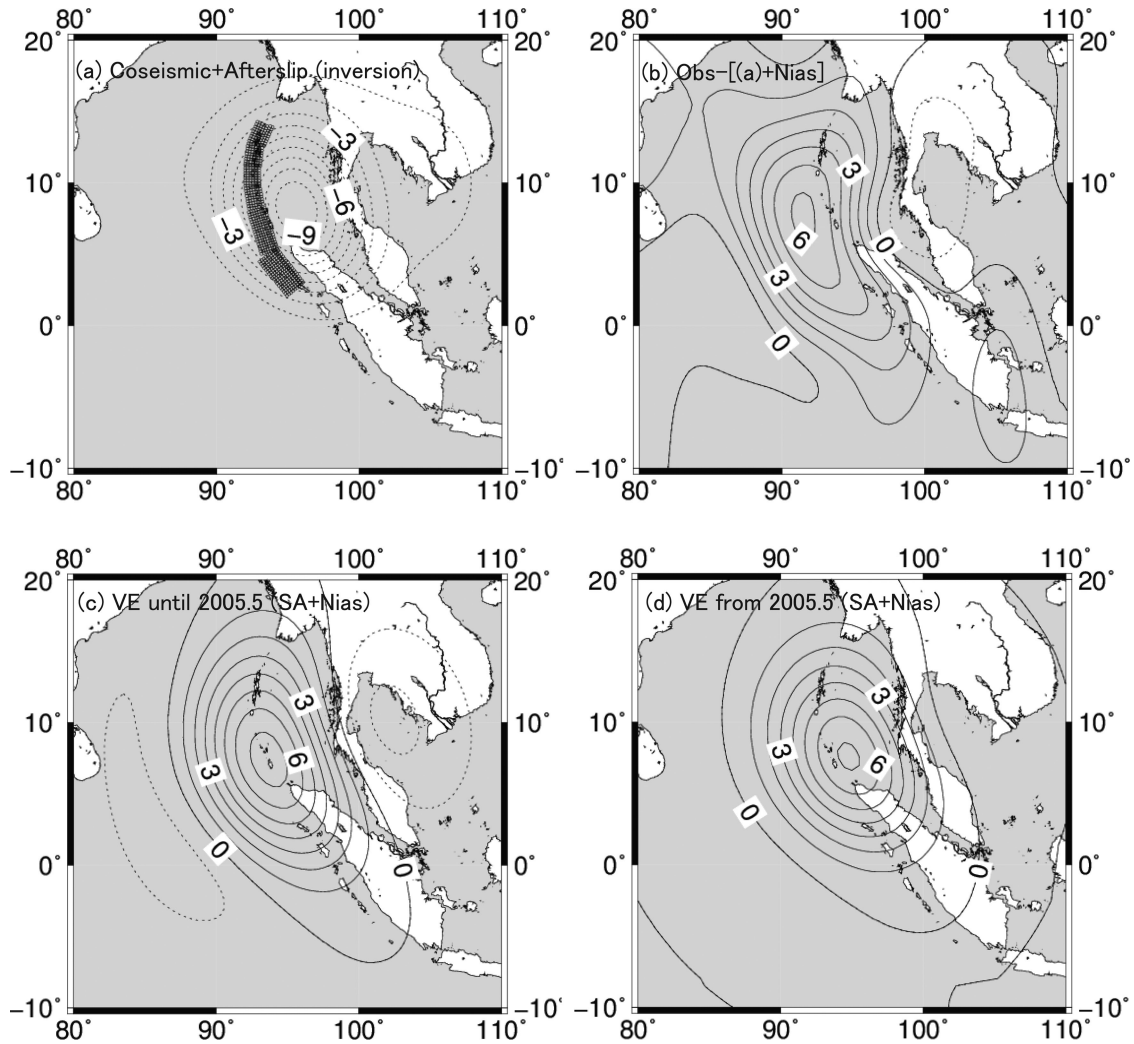


**Figure 9.** (a) The gravity change predicted from the fault model determined by the inversion of the GRACE data. This fault model considers coseismic slip and afterslip until 2005.5. (b) The pattern obtained by subtracting the change in (a) and the coseismic change by the Nias event (Fig. C1) from the observed change (Fig. 5d). (c and d) The transient gravity changes caused by viscoelastic relaxation due to the 2004 Sumatra and the 2005 Nias events during the period before 2005.5 and the period from 2005.5 to 2011.5. The units are  $\mu\text{Gal}$ , the contour interval is  $1 \mu\text{Gal}$  and dotted lines denote negative changes.

appears that the model based on Burgers rheology better explains the observed pattern shown in Fig. 5(d) than the model where only coseismic slip and afterslip is considered (Fig. 9a).

By subtracting the pattern of Fig. 10(a) from Fig. 5(b), the misfit between the model and the observation is drawn in Fig. 10(b). A negative gravity change of approximately  $3 \mu\text{Gal}$  remain above the east of the source area, which cannot be explained by the model. To the southwest of the source area, a broader positive anomaly of approximately  $1 \mu\text{Gal}$  is observed. This pattern with the larger negative and the smaller positive changes is also observed in the difference between the model and the observation at 2011.5 (Fig. 10c). This pattern can be explained by an additional afterslip (Fig. 10d). The change in Fig. 10(d) is computed using the fault model determined by the inversion (Fig. 9a) but with the slips for depths shallower than 30 km set to zero. The pattern in Fig. 10(d) appears to reproduce the patterns in plots b and c, which indicates that the model can be further improved by including this additional afterslip in the fault model. The validity of the moment release by this additional afterslip is discussed in Section 4. Fig. 11 shows time-series plots of the model excluding and including the additional afterslip (the red and the purple lines, respectively). The observed data are also

superimposed by blue points. The observed value at 2004.5 is taken as zero because it represents the reference state before the earthquake. By considering the offset by the additional afterslip to the coseismic step, the agreement with the observation becomes much better at the east side of the source, where the remaining negative signal (Fig. 10b) was larger (Figs 11b–d).

### 3.5 Influence of the subducting slab

Finally, effects due to the presence of an elastic subducting slab on viscoelastic relaxation is estimated. Figs 12(a) and (b) show the difference between 1-D and 3-D models at 2005.5 and 2011.5, respectively. The 1-D model is the same as before. In the 3-D model, the lateral heterogeneity in viscosity that is shown in Fig. 12(c) is considered. The elastic slab has the same thickness as the lithosphere (70 km) and subducts towards the direction normal to the average strike angle of the faults ( $330^\circ$ ). The width of the slab is  $\pm 3000$  km from the centre of the source in the direction of  $N30^\circ W$  and  $N150^\circ E$ . In the 1-D model, gravity increases above the source area (Figs 9c and d). Fig. 12(a) indicates that the increase is

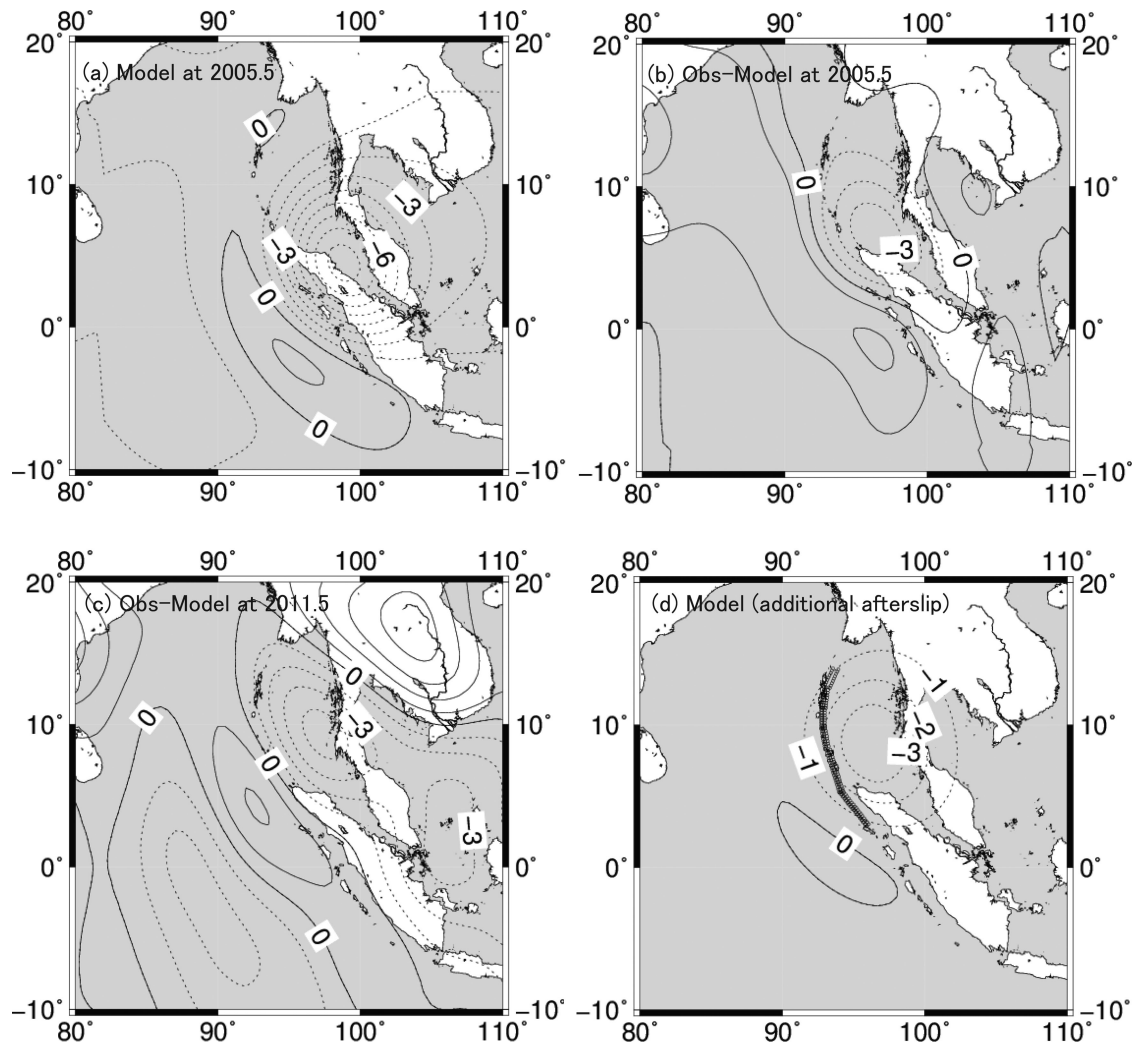


**Figure 10.** (a) The gravity change at 2005.5, calculated with the fault model determined by inversion of the GRACE data. All mechanisms of coseismic slip, afterslip and viscoelastic relaxation of the Sumatra event and of the Nias events are included. (b) The misfit of (a) against Fig. 5(d). (c) The misfit of the model against the observed gravity field at 2011.5. (d) The change due to an additional afterslip distributed in depths from 30 to 50 km. The units are  $\mu\text{Gal}$ , the contour interval is 1  $\mu\text{Gal}$  and dotted lines denote negative changes.

reduced by 10–15 per cent in the presence of the slab. Moreover, the gravity decrease to the northeast in Fig. 9(c) is also weakened by approximately 20 per cent. Southwest of the source area, significant differences are not observed between the 1-D and the 3-D models. Beneath the source area and in the deeper portion in the northeast, elasticity of the slab reduces the effective viscous dissipation within the asthenosphere, which decreases the amplitudes of the gravity changes at the Earth surface. The same feature is also observed in the incompressible case (Tanaka *et al.* 2009). The difference due to the slab is smaller than 1  $\mu\text{Gal}$  at the wavelength of 500 km, which does not affect the above-mentioned inference regarding the mechanisms of the post-seismic deformation.

#### 4 DISCUSSION AND CONCLUSIONS

By analysing the Release-05 GRACE level-2 products, co- and post-seismic gravity changes due to the 2004 Sumatra–Andaman Earthquake were re-evaluated. In this analysis, annual averages of gravity changes from the different GRACE data analysis centres and ocean and hydrological models were used to obtain more

robust spatial patterns of the co- and post-seismic gravity changes. Consequently, an obvious difference was revealed between the spatial pattern of the short-term change until 2005.5 (including the coseismic effect) and that of the long-term change after 2005.5. Spatial patterns in the gravity variations should be more effective to discern differences in the mechanisms than in the geoid height changes because the gravity variations reflect shorter-wavelength deformations. To utilize this feature, a new theoretical computation approach was developed, with which the spatial patterns of gravity changes derived from various co- and post-seismic deformation mechanisms were presented including coseismic slip, afterslip, viscoelastic relaxation, poroelastic rebound and splay fault.

The applied computational method is an expansion of the spectral-finite element approach of Martinec (2000) and Tanaka *et al.* (2009) to compute co- and post-seismic deformation in a self-gravitating Maxwell viscoelastic spherical Earth with lateral heterogeneities in viscosity, where compressibility is considered in the governing equations and the material law was extended to the second order linear Burgers rheology. Through this extension, the approach has yielded practical applications. The main advantage of this approach with respect to usually applied finite element models

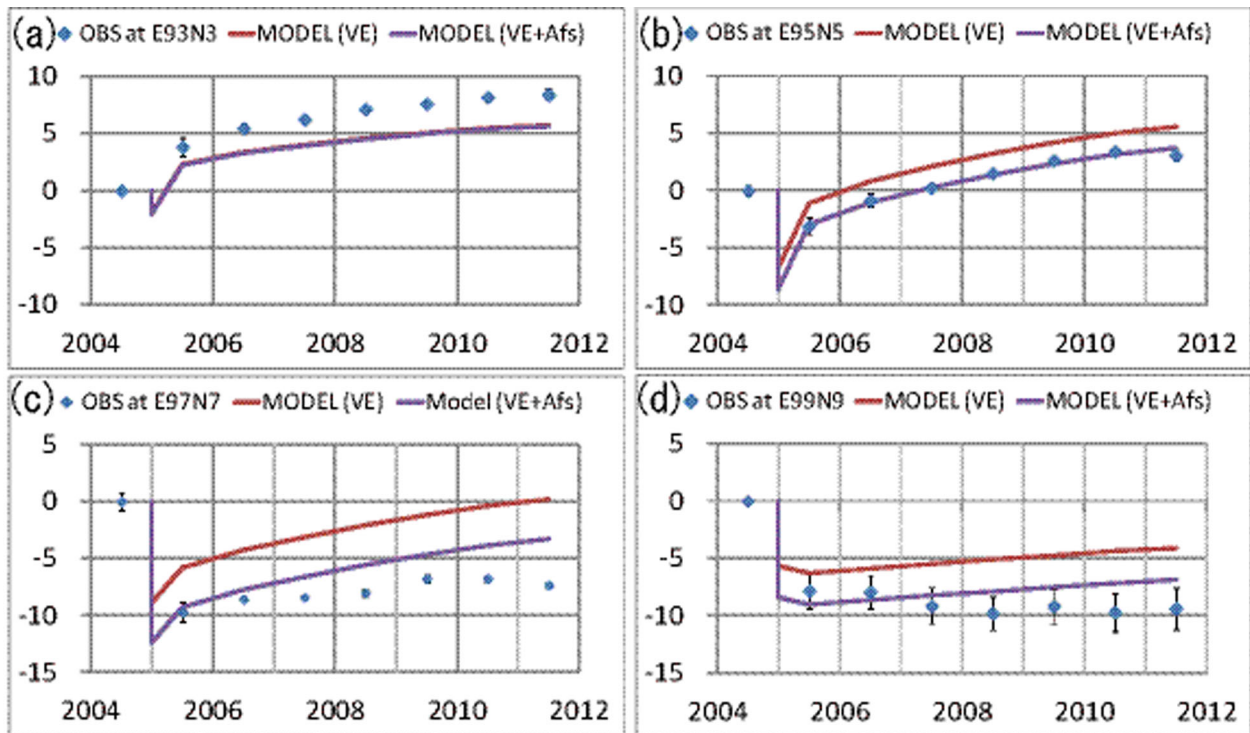


Figure 11. A comparison between the model (red and purple lines) and the observation (blue points) in time-series plots. The unit on the vertical axis is  $\mu\text{Gal}$ .

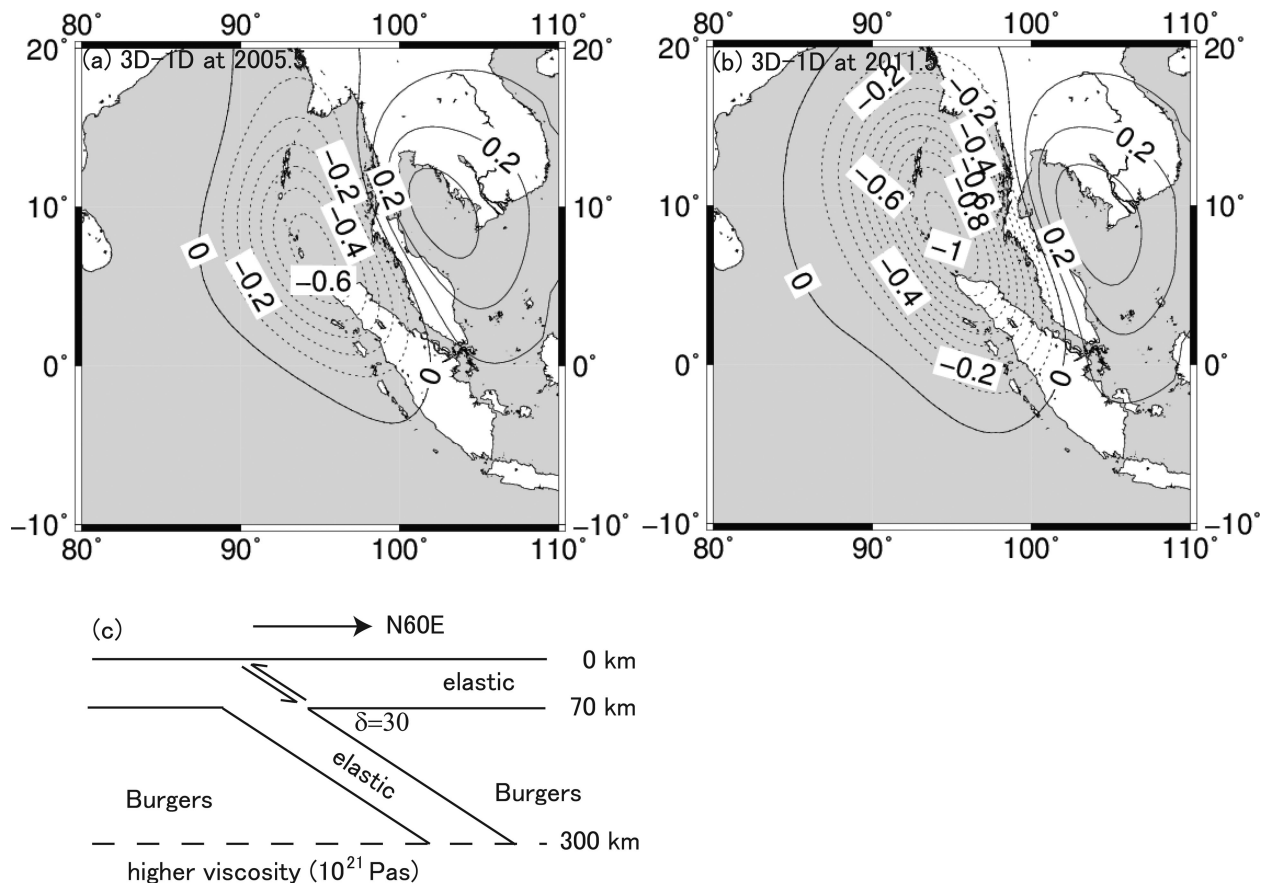
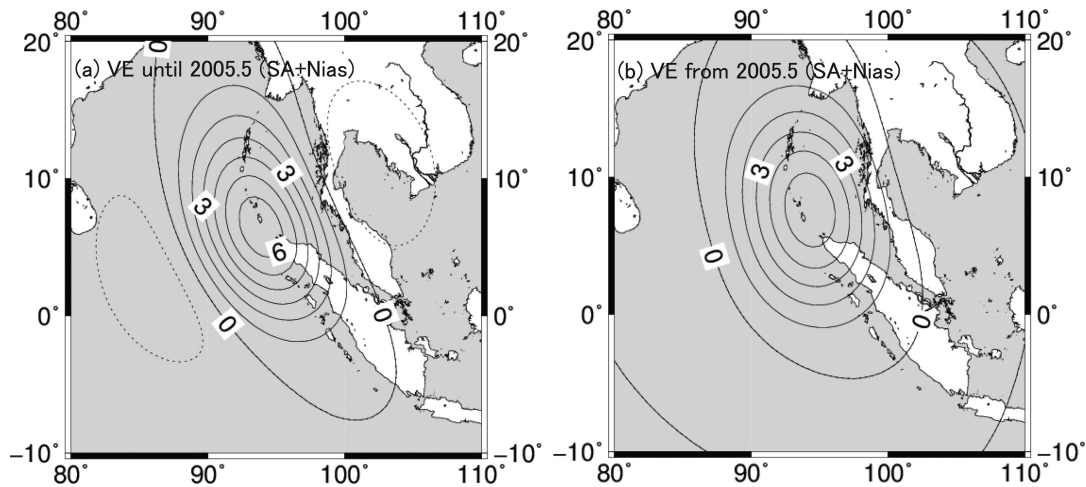


Figure 12. The effect of the slab on viscoelastic relaxation. The differences are obtained by subtracting the gravity change calculated for the 1-D model excluding the slab from the change computed for the 3-D model including the slab. The differences at 2005.5 and 2011.5 are shown in (a) and (b), respectively. (c) The cross section of the 3-D viscosity structure along the direction of  $\text{N}60^\circ\text{E}$ . The dip angle of the elastic slab is fixed at  $30^\circ$ . The units are  $\mu\text{Gal}$ , the contour interval is  $0.1 \mu\text{Gal}$  and dotted lines denote negative changes.



**Figure 13.** The gravity change due to the viscoelastic relaxation that is computed for the fault model determined by the GNSS data (Banerjee *et al.* 2007). The viscosity structure is the same as in the previous case excluding the slab. (a) and (b) show the change until 2005.5 and the change from 2005.5 to 2011.5, respectively. The units are  $\mu\text{Gal}$ , the contour interval is 1  $\mu\text{Gal}$  and dotted lines denote negative changes.

is that the effects of sphericity and self-gravitation are considered consistently by solving the global deformation problem. Computational results are represented in form of Stokes' coefficients, which can easily be compared with GRACE data that are provided in the same format. In this sense, we rate this method superior to known flat-Earth approaches, although the method is restricted to flat terrain and radial symmetry with respect to density and elasticity.

The comparisons between the GRACE data and the discussed deformation mechanisms indicated that (i) the fault models determined by the GNSS and the seismic wave observations in previous studies were not necessarily consistent with the GRACE gravity fields, (ii) the spatial pattern observed during the period until 2005.5 could be interpreted as a superposition of coseismic slip, afterslip and short-term viscoelastic relaxation due to a Burgers rheology, (iii) the pattern observed during the 2005.5–2011.5 period was mainly caused by viscoelastic relaxation and (iv) the 3-D effect on viscoelastic relaxation by considering an elastic slab has a minor impact on the assessment of the mechanisms.

One limitation of the present study is that the coseismic slip is simultaneously inferred with the afterslip during the period until 2005.5 because the GNSS data are not used in the analysis. Our results show that the moment magnitude released until 2005.5, including the contributions from the coseismic slip and the additional afterslip, is  $M_w 9.2$  for  $2.3 (= 1.8 + 0.54) \times 10^{12} \text{ m}^3$ , which is 1.5 times larger than the coseismic moment release determined by the GNSS data (Banerjee *et al.* 2007) ( $M_w 9.0$  corresponding to  $1.5 \times 10^{12} \text{ m}^3$  when  $\mu_c = 30 \text{ GPa}$ ). When subtracting this coseismic effect from the moment release estimated by the GRACE data, the release by the afterslip until 2005.5 becomes  $M_w 8.9$ . From the GNSS data, Hashimoto *et al.* (2006) and Banerjee *et al.* (2007) estimated the moment release by the afterslip that occurred during the first 3 months and the first 50 d after the 2004 Sumatra event as  $M_w 8.7$  and 8.6 (corresponding to  $\sim 3 \times 10^{11} \text{ m}^3$  when  $\mu_c = 30 \text{ GPa}$ ), respectively. The values of those studies were estimated without considering the short-term viscoelastic relaxation. Pollitz *et al.* (2006) explained the short-term GPS data almost solely by the Burgers model. Paul *et al.* (2007) showed that the moment release by afterslip until 2 yr after the Sumatra event may be larger than  $M_w 7.5$  by constructing a model where viscoelastic relaxation and afterslip were combined. Therefore, afterslip appears to be not yet robustly constrained even when using the GNSS data during this

period. Our finding based on GRACE data reveals that the observed spatial patterns cannot be interpreted solely by afterslip or viscoelastic relaxation, although the amount and the spatial distribution of the afterslip and viscosity values can change slightly. The necessity of both afterslip and Burgers rheology agrees with the conclusion of Panet *et al.* (2010) based on the GNSS and GRACE data. The inferred viscosity ( $\nu_1 = 6 \times 10^{18}$ ,  $\nu_2 = 6 \times 10^{17} \text{ Pa s}$ ) is also similar to their result ( $\nu_1 = 8 \times 10^{18}$ ,  $\nu_2 = 4 \times 10^{17} \text{ Pa s}$ ).

The moment release by afterslip during the period from 2005.5 to 2011.5 can also be estimated if viewing the gravity difference (i.e. Fig. 10c minus Fig. 10b) as significant. Amplitudes of the positive and the negative anomalies in Fig. 10(b) (+1 and  $-3 \mu\text{Gal}$ , respectively) appear to be increased by approximately 1  $\mu\text{Gal}$  in Fig. 10(c). Therefore, if we assume that one-third of the additional afterslip occurred during the 2005.5–2011.5 period, the moment release from 2005.5 to 2011.5 becomes  $M_w 8.4$ . Studies have revealed that afterslip occurred in periods between 2005.5 and 2011.5. Paul *et al.* (2012) stated that inclusion of afterslip at depths immediately below the downdip terminus of coseismic rupture can explain the GNSS data obtained from 4 to 6 yr after the event better than models where only viscoelastic flow is considered. Panet *et al.* (2010) showed that an  $M_w 8.2$  afterslip which is distributed at depths from 30 to 85 km is necessary to explain the misfit between the viscoelastic relaxation model and the observed geoid data during the period from 2005 April to 2007 September. A physical mechanism to generate such a deep slip is proposed in Mikhailov *et al.* (2013). Our results indicate that afterslip is distributed at depths from 30 to 50 km, as was originally proposed for the inference of afterslip by GNSS data (Banerjee *et al.* 2007). Although our slip distribution depths differ from those in Panet *et al.* (2010), the moment magnitude estimated from the GRACE data is comparable. A possible reason for this is the choice of coseismic fault models. Panet *et al.* (2010) used the coseismic fault model determined by the GNSS data of Banerjee *et al.* (2007), and analysed the post-seismic geoid change that occurred only after 2005.5. In our study, the coseismic fault model was redetermined to best account for the GRACE data and GNSS data were not employed.

From the above discussion, there are still uncertainties in determining the afterslip between studies using GNSS and GRACE data. However, it is likely that viscoelastic relaxation was occurring (at least after the year 2005.5 if Burgers rheology is replaced by

Maxwell rheology). Fig. 13 shows the viscoelastic relaxation patterns obtained for the fault model determined by the GNSS data. Because the contribution of the viscoelastic relaxation is larger than the contribution of afterslip, the model can explain the observed spatial patterns of Fig. 9(b) (shorter-term) and Fig. 6(a) (longer-term) to the same extent as Figs 9(c) and (d) can do, which means that the results from the GNSS and the GRACE are consistent with respect to the presence of a viscoelastic relaxation mechanism and apart from the resultant differences in afterslip distributions.

To resolve discrepancies in afterslip distributions, a simultaneous inversion of GNSS and GRACE data is required. To enable the consideration of the GNSS data, a code is under development to compute the displacement field, including the effects from the shorter-wavelength deformation corresponding to higher-order spherical harmonic degrees. However, it has been demonstrated that valuable information to separate post-seismic deformation mechanisms can be obtained even from GRACE data only. A web application program based on the presented code for the computation of gravity changes for a spherically symmetric model will soon be available at the web site <http://www.eri.u-tokyo.ac.jp/y-tanaka/>. It is hoped that the computation method will be useful for investigating the post-seismic deformation mechanisms of recent mega-thrust events.

## ACKNOWLEDGEMENTS

GMT (Wessel & Smith 1991) was used to generate the figures in this paper. The manuscript was greatly improved by the comments from the two anonymous reviewers.

## REFERENCES

- Ammon, C.J. *et al.*, 2005. Rupture process of the 2004 Sumatra-Andaman earthquake, *Science*, **308**, 1133–1139.
- Banerjee, P., Pollitz, F. & Burgmann, R., 2005. The size and duration of the Sumatra-Andaman Earthquake from far-field static offsets, *Science*, **308**, 1769–1772.
- Banerjee, P., Pollitz, F., Nagarajan, G. & Burgmann, R., 2007. Co-seismic slip distributions of the 26 December 2004 Sumatra-Andaman and 28 March 2005 Nias earthquakes from GPS static offsets, *Bull. seism. Soc. Am.*, **97**, S86–S102.
- Barbot, S. & Fialko, Y., 2010. A unified continuum representation of post-seismic relaxation mechanisms: semi-analytic models of afterslip, poroelastic rebound and viscoelastic flow, *Geophys. J. Int.*, **182**, 1124–1140.
- Broerse, D.B.T., Vermeersen, L.L.A., Riva, R.E.M. & van der Wal, W., 2011. Ocean contribution to co-seismic crustal deformation and geoid anomalies: application to the 2004 December 26 Sumatra-Andaman earthquake, *Earth planet. Sci. Lett.*, **305**, 341–349.
- Bürgmann, R. & Dresen, G., 2008. Rheology of the lower crust and upper mantle: evidence from rock mechanics, geodesy and field observations, *Annu. Rev. Earth planet. Sci.*, **36**, 531–567.
- Cambiotti, G. & Sabadini, R., 2010. The compressional and compositional stratifications in Maxwell Earth models: the gravitational overturning and the long period tangential flux, *Geophys. J. Int.*, **180**, 475–500.
- Cambiotti, G., Barletta, V.R., Bordononi, A. & Sabadini, R., 2009. A comparative analysis of the solutions for a Maxwell Earth: the role of the advection and buoyancy force, *Geophys. J. Int.*, **176**, 995–1006.
- Cambiotti, G., Bordononi, A., Sabadini, R. & Colli, L., 2011. GRACE gravity data help constraining seismic models of the 2004 Sumatran earthquake, *J. geophys. Res.*, **116**, B10403, doi:10.1029/2010JB007848.
- Chen, F. *et al.*, 1996. Modeling of land-surface evaporation by four schemes and comparison with FIFE observations. *J. geophys. Res.*, **101**, 7251–7268.
- Chen, J.L., Wilson, C.R., Tapley, B.D. & Grand, S., 2007. GRACE detects co-seismic and post-seismic deformation from the Sumatra-Andaman earthquake, *Geophys. Res. Lett.*, **34**, L13302, doi:10.1029/2007GL030356.
- Chlieh, M. *et al.*, 2007. Co-seismic slip and afterslip of the great Mw 9.15 Sumatra-Andaman earthquake of 2004, *Bull. seism. Soc. Am.*, **97**, S152–S173.
- Cohen, S.C., 1994. Evaluation of the importance of model features for cyclic deformation due to dip-slip faulting, *Geophys. J. Int.*, **119**, 831–841.
- Dahlen, F.A., 1974. On the static deformation of an Earth model with a fluid core, *Geophys. J. R. astr. Soc.*, **36**, 461–485.
- Dai, Y. *et al.*, 2003. The Common Land Model (CLM), *Bull. Am. Meteorol. Soc.*, **84**, 1013–1023.
- de Linage, C., Rivera, L., Hinderer, J., Boy, J.-P., Rogister, Y., Lambotte, S. & Biancale, R., 2009. Separation of co-seismic and post-seismic gravity changes for the 2004 Sumatra-Andaman earthquake from 4.6 yr of observations and modeling of the co-seismic change by normal-modes summation, *Geophys. J. Int.*, **176**, 695–714.
- Dziewonski, A.M. & Anderson, A., 1981. Preliminary reference earth model, *Phys. Earth planet. Inter.*, **25**, 297–356.
- Dow, J.M., Neilan, R.E. & Rizos, C., 2009. The International GNSS Service in a changing landscape of Global Navigation Satellite Systems, *J. Geod.*, **83**, 191–198.
- Fu, G. & Sun, W., 2008. Surface co-seismic gravity changes caused by dislocations in a 3-D heterogeneous earth, *Geophys. J. Int.*, **172**, 479–503.
- Gilbert, F. & Backus, G., 1968. Elastic-gravitational vibrations of a radially stratified sphere, in *Dynamics of Structured Solids*, pp. 82–95, ed. Herrmann, G., American Society of Mechanical Engineers.
- Han, S.C., Shum, C.K., Bevis, M., Ji, C. & Kuo, C.Y., 2006. Crustal dilatation observed by GRACE after the 2004 Sumatra-Andaman earthquake, *Science*, **313**, 658–666.
- Han, S.C., Sauber, J., Luthcke, S.B., Ji, C. & Pollitz, F.F., 2008. Implications of post-seismic gravity change following the great 2004 Sumatra-Andaman earthquake from the regional harmonic analysis of GRACE intersatellite tracking data, *J. geophys. Res.*, **113**, B11413, doi:10.1029/2008JB005705.
- Hanyk, L., Moser, J., Yuen, D.A. & Matyska, C., 1995. Time-domain approach for the transient responses in stratified viscoelastic Earth models, *Geophys. Res. Lett.*, **22**, 1285–1288.
- Hasegawa, T., Fukuda, Y., Yamamoto, K. & Nakaegawa, T., 2009. The 2006 Australian drought detected by GRACE, in *Headwaters to the Ocean*, pp. 363–367, eds Taniguchi, M. *et al.*, Taylor & Francis Group.
- Hashimoto, M., Choosakul, N., Hashizume, M., Takemoto, S., Takiguchi, H., Fukuda, Y. & Fujimori, K., 2006. Crustal deformations associated with the great Sumatra-Andaman earthquake deduced from continuous GPS observation, *Earth Planets Space*, **58**, 127–139.
- Hoechner, A., Sobolev, S.V., Einarsson, I. & Wang, R., 2011. Investigation on afterslip and steady state and transient rheology based on post-seismic deformation and geoid change caused by the Sumatra 2004 earthquake, *Geochem. Geophys. Geosyst.*, **12**, Q07010, doi:10.1029/2010GC003450.
- Hu, Y., Wang, K., He, J., Klotz, J. & Khazaradze, G., 2004. Three-dimensional viscoelastic finite element model for post-seismic deformation of the great 1960 Chile earthquake, *J. geophys. Res.*, **109**, B12403, doi:10.1029/2004JB003163.
- Hughes, K.L.H., Masterlark, T. & Mooney, W.D., 2010. Poroelastic stress-triggering of the 2005 M8.7 Nias earthquake by the 2004 M9.2 Sumatra-Andaman earthquake, *Earth planet. Sci. Lett.*, **293**, 289–299.
- Jekeli, C., 1981. Alternative methods to smooth the Earth's gravity field, *Rep. 327, Dep. Of Geod. Sci. and Surv.*, Ohio State Univ., Columbus.
- Jonsson, S., Segall, P., Pedersen, R. & Bjornsson, G., 2003. Post-earthquake ground movements correlated to pore-pressure transients, *Nature*, **424**, 179–183.
- Klemann, V., Ivins, E., Martinec, Z. & Wolf, D., 2007. Models of active glacial isostasy roofing warm subduction: case of the South Patagonian Ice Field, *J. geophys. Res.*, **112**, B09405, doi:10.1029/2006JB004818.
- Klemann, V., Martinec, Z. & Ivins, E.R., 2008. Glacial isostasy and plate motion, *J. Geodyn.*, **46**, 95–103.

- Koren, V., Schaake, J., Mitchell, K., Duan, Q.Y., Chen, F. & Baker, J.M., 1999. A parameterization of snowpack and frozen ground intended for NCEP weather and climate models. *J. geophys. Res.*, **104**, 19 569–19 585.
- Love, A.E.H., 1911. *Some Problems of Geodynamics*, pp. 180, Cambridge University Press
- Marone, C., Scholz, C.H. & Bilham, R., 1991. On the mechanics of earthquake afterslip. *J. geophys. Res.*, **96**, 8441–8452.
- Martinec, Z., 2000. Spectral-finite element approach to three-dimensional viscoelastic relaxation in a spherical Earth. *Geophys. J. Int.*, **142**, 117–141.
- Masterlark, T. & Hughes, K.L.H., 2008. Next generation of deformation models for the 2004 M9 Sumatra-Andaman earthquake. *Geophys. Res. Lett.*, **35**, L19310, doi:10.1029/2008GL035198.
- Matsuo, K. & Heki, K., 2011. Co-seismic gravity changes of the 2011 Tohoku-Oki Earthquake from satellite gravimetry. *Geophys. Res. Lett.*, **38**, L00G12, doi:10.1029/2011GL049018.
- Mikhailov, V., Lyakhovskiy, V., Panet, I., van Dinther, Y., Diament, M., Gerya, T., deViron, O. & Timoshkina, E., 2013. Numerical modeling of post-seismic rupture propagation after the Sumatra 26.12.2004 earthquake constrained by GRACE gravity data. *Geophys. J. Int.*, **194**(2), 640–650.
- Ogawa, R. & Heki, K., 2007. Slow post-seismic recovery of geoid depression formed by the 2004 Sumatra-Andaman Earthquake by mantle water diffusion. *Geophys. Res. Lett.*, **34**, L06313, doi:10.1029/2007GL029340.
- Okada, Y., 1985. Surface deformation due to shear and tensile faults in a half-space. *Bull. seism. Soc. Am.*, **75**, 1435–1154.
- Okubo, S., 1993. Reciprocity theorem to compute the static deformation due to a point dislocation buried in a spherically symmetric earth. *Geophys. J. Int.*, **115**, 921–928.
- Ozawa, S., Kaidzu, M., Murakami, M., Imakiire, T. & Hatanaka, Y., 2004. Co-seismic and post-seismic crustal deformation after the M8 Tokachi-oki earthquake in Japan. *Earth Planets Space*, **56**, 675–680.
- Ozawa, S., Nishimura, T., Suito, H., Kobayashi, T., Tobita, M. & Imakiire, T., 2011. Co-seismic and post-seismic slip of the 2011 magnitude-9 Tohoku-Oki earthquake. *Nature*, **475**, 373–376.
- Panet, I. et al., 2007. Co-seismic and post-seismic signatures of the Sumatra 2004 December and 2005 March earthquakes in GRACE satellite gravity. *Geophys. J. Int.*, **171**, 177–190.
- Panet, I., Pollitz, F., Mikhailov, V., Diament, M., Banerjee, P. & Grijalva, K., 2010. Upper mantle rheology from GRACE and GPS post-seismic deformation after the 2004 Sumatra-Andaman earthquake. *Geochem. Geophys. Geosyst.*, **11**, Q06008, doi:10.1029/2009GC002905.
- Paul, J., A. Lowry, R., Bilham, R., Sen, S. & Smalley, R. Jr, 2007. Post-seismic deformation of the Andaman Islands following the 26 December, 2004 Great Sumatra-Andaman earthquake. *Geophys. Res. Lett.*, **34**, L19309, doi:10.1029/2007GL031024.
- Paul, J., Rajendran, C.P., Lowry, A.R., Andrade, V. & Rajendran, K., 2012. Andaman post-seismic deformation observations: still slipping after all these years?. *Bull. seism. Soc. Am.*, **102**(1), 343–351.
- Peltier, W.R., 1974. The impulse response of a Maxwell Earth. *Rev. Geophys. Space Phys.*, **12**, 649–669.
- Peltier, W.R., 1981. Ice age geodynamics. *Ann. Rev. Earth. planet. Sci.*, **9**, 199–225.
- Peltzer, G., Rosen, P., Rogez, F. & Hudnut, K., 1998. Poroelastic rebound along the Landers 1992 earthquake surface rupture. *J. geophys. Res.*, **103**, 30 131–30 145.
- Piersanti, A., Spada, G., Sabadini, R. & Bonafede, M., 1995. Global post-seismic deformation. *Geophys. J. Int.*, **120**, 544–566.
- Pollitz, F.F., 1997. Gravitational viscoelastic post-seismic relaxation on a layered spherical Earth. *J. geophys. Res.*, **102**, 17 921–17 941.
- Pollitz, F.F., 2003. Post-seismic relaxation theory on a laterally heterogeneous viscoelastic model. *Geophys. J. Int.*, **155**, 57–78.
- Pollitz, F.F., Burgmann, R. & Banerjee, P., 2006. Post-seismic relaxation following the great 2004 Sumatra-Andaman earthquake on a compressible self-gravitating Earth. *Geophys. J. Int.*, **167**, 397–420.
- Pollitz, F., Banerjee, P., Grijalva, K., Nagarajan, B. & Bürgmann, R., 2008. Effect of 3-D viscoelastic structure on post-seismic relaxation from the 2004 M=9.2 Sumatra earthquake. *Geophys. J. Int.*, **173**, 189–204.
- Press, W.H., Teukolsky, S.A., Vetterling, W.T. & Flannery, B.P., 1992. *Numerical Recipes in Fortran. The Art of Scientific Computing*, Cambridge Univ. Press.
- Scholz, C.H., 1998. Earthquakes and friction laws. *Nature*, **391**, 37–42.
- Sun, W. & Okubo, S., 1993. Surface potential and gravity changes due to internal dislocations in a spherical Earth. I. Theory for a point dislocation. *Geophys. J. Int.*, **114**, 569–592.
- Swenson, S. & Wahr, J., 2006. Post-processing removal of correlated errors in GRACE data. *Geophys. Res. Lett.*, **33**, L08402, doi:10.1029/2005GL025285.
- Takeuchi, H. & Saito, M., 1972. Seismic surface waves. *Methods Comput. Phys.*, **11**, 217–295.
- Tanaka, Y., Okuno, J. & Okubo, S., 2006. A new method for the computation of global viscoelastic post-seismic deformation in a realistic Earth model (I)—vertical displacement and gravity variation. *Geophys. J. Int.*, **164**, 273–289.
- Tanaka, Y., Okuno, J. & Okubo, S., 2007. A new method for the computation of global viscoelastic post-seismic deformation in a realistic earth model, (II)—horizontal displacement. *Geophys. J. Int.*, **170**, 1031–1052.
- Tanaka, Y., Klemann, V., Fleming, K. & Martinec, Z., 2009. Spectral finite element approach to post-seismic deformation in a viscoelastic self-gravitating spherical Earth. *Geophys. J. Int.*, **176**, 715–739.
- Tanaka, Y., Klemann, V., Martinec, Z. & Riva, R.E.M., 2011. Spectral-finite element approach to viscoelastic relaxation in a spherical compressible Earth: application to GIA modeling. *Geophys. J. Int.*, **184**, 220–234.
- Tapley, B., Bettadpur, S., Ries, J., Thompson, P. & Watkins, M., 2004. GRACE measurements of mass variability in the Earth system. *Science*, **305**, 503–505.
- Thatcher, W. & Rundle, J.B., 1984. A viscoelastic coupling model for the cyclic deformation due to periodically repeated earthquakes at subduction zones. *J. geophys. Res.*, **89**, 7631–7640.
- Tsai, V.C., Nettles, M., Ekström, G. & Dziewonski, A.M., 2005. Multiple CMT source analysis of the 2004 Sumatra earthquake. *Geophys. Res. Lett.*, **32**, L17304, doi:10.1029/2005GL023813.
- Vigny, C. et al., 2011. The 2010 Mw 8.8 Maule Megathrust Earthquake of Central Chile, monitored by GPS. *Science*, **332**, 1417–1421.
- Wang, K., He, J., Dragert, H. & James, T.S., 2001. Three-dimensional viscoelastic interseismic deformation model for the Cascadia subduction zone. *Earth planets Space*, **53**, 295–306.
- Wang, K., Hu, Y. & He, J., 2012a. Deformation cycles of subduction earthquakes in a viscoelastic Earth. *Nature*, **484**, 327–332.
- Wang, L. et al., 2012b. Co-seismic slip of the 2010 Mw 8.8 Great Maule, Chile, earthquake quantified by the inversion of GRACE observations. *Earth planet. Sci. Lett.*, **335–336**, 167–179.
- Wessel, P. & Smith, W.H.F., 1991. Free software helps map and display data. *EOS, Trans. Am. geophys. Un.*, **72**, 441.
- Wu, P. & Peltier, W.R., 1982. Viscous gravitational relaxation. *Geophys. J. R. astr. Soc.*, **70**, 435–485.

## APPENDIX A: THE SOURCE CONDITION

The double-couple forces equivalent to a point dislocation are expressed by combining point forces. Point forces are expanded on a sphere in spherical harmonics. A point force with a unit magnitude applied at the location  $(r_0, \theta_0, \varphi_0)$  can be written in terms of vector spherical

harmonics,  $\mathbf{S}_{jm}^{(\lambda)}$ , as

$$\mathbf{f}(r, \theta, \varphi) = \frac{\delta(r-r_0)}{r_0^2} \sum_{j,m} \left( v_r Y_{jm}^*(\theta, \varphi)|_{\theta_0, \varphi_0} \mathbf{S}_{jm}^{(-1)}(\theta, \varphi) + \left[ v_\theta \frac{\partial Y_{jm}^*(\theta, \varphi)}{\partial \theta} + v_\varphi \frac{1}{\sin \theta} \frac{\partial Y_{jm}^*(\theta, \varphi)}{\partial \varphi} \right]_{\theta_0, \varphi_0} \mathbf{S}_{jm}^{(1)}(\theta, \varphi) + \left[ -v_\theta \frac{1}{\sin \theta} \frac{\partial Y_{jm}^*(\theta, \varphi)}{\partial \varphi} + v_\varphi \frac{\partial Y_{jm}^*(\theta, \varphi)}{\partial \theta} \right]_{\theta_0, \varphi_0} \mathbf{S}_{jm}^{(0)}(\theta, \varphi) \right) \quad (\text{A1})$$

(eq. 257 in Takeuchi & Saito 1972). Here,  $v_r$ ,  $v_\theta$  and  $v_\varphi$  represent the three components of the unit direction vector of the prescribed force,  $\mathbf{f}$ , at  $\theta = \theta_0$ ,  $\varphi = \varphi_0$ , and the asterisk denotes complex conjugate.

By superposition of point forces, single-couple forces corresponding to each fault mechanism can be obtained. The variation in the work for each type of single-couple forces can be written as

$$\delta \mathcal{W}^{(A)} = -\frac{\mu_k \Delta u \Delta A}{r_0} \sin 2\delta \sin \alpha \sum_{j,m} \left[ \sin^2 \Theta \frac{\partial^2 Y_{jm}^*(\theta, \varphi)}{\partial \theta^2} + \sin \Theta \cos \Theta \left( \frac{\partial}{\partial \theta} \left( \frac{1}{\sin \theta} \frac{\partial Y_{jm}^*(\theta, \varphi)}{\partial \varphi} \right) + \frac{1}{\sin \theta} \frac{\partial^2 Y_{jm}^*(\theta, \varphi)}{\partial \theta \partial \varphi} \right) + \cos^2 \Theta \frac{1}{\sin^2 \theta} \frac{\partial^2 Y_{jm}^*(\theta, \varphi)}{\partial \varphi^2} \right]_{\theta_0, \varphi_0} \delta V_{jm}^k, \quad (\text{A2})$$

$$\delta \mathcal{W}^{(AT)} = \frac{\mu_k \Delta u \Delta A}{r_0} \sin 2\delta \sin \alpha \sum_{j,m} \left[ \sin^2 \Theta \frac{\partial}{\partial \theta} \left( \frac{1}{\sin \theta} \frac{\partial Y_{jm}^*(\theta, \varphi)}{\partial \varphi} \right) + \sin \Theta \cos \Theta \times \left( -\frac{\partial^2 Y_{jm}^*(\theta, \varphi)}{\partial \theta^2} + \frac{1}{\sin^2 \theta} \frac{\partial^2 Y_{jm}^*(\theta, \varphi)}{\partial \varphi^2} \right) - \cos^2 \Theta \frac{1}{\sin \theta} \frac{\partial^2 Y_{jm}^*(\theta, \varphi)}{\partial \theta \partial \varphi} \right]_{\theta_0, \varphi_0} \delta W_{jm}^k, \quad (\text{A3})$$

$$\delta \mathcal{W}^{(B)} = -\frac{\mu_k \Delta u \Delta A}{r_0} \sum_{j,m} \left( \cos 2\delta \sin \alpha \left[ \sin \Theta \frac{\partial Y_{jm}^*(\theta, \varphi)}{\partial \theta} + \cos \Theta \frac{1}{\sin \theta} \frac{\partial Y_{jm}^*(\theta, \varphi)}{\partial \varphi} \right]_{\theta_0, \varphi_0} + \cos \delta \cos \alpha \left[ -\sin \Theta \frac{1}{\sin \theta} \frac{\partial Y_{jm}^*(\theta, \varphi)}{\partial \varphi} + \cos \Theta \frac{\partial Y_{jm}^*(\theta, \varphi)}{\partial \theta} \right]_{\theta_0, \varphi_0} \right) \delta U_{jm}^k, \quad (\text{A4})$$

$$\delta \mathcal{W}^{(C+)} = \frac{\mu_k \Delta u \Delta A}{r_0} \sin 2\delta \sin \alpha \frac{r_k}{r_{k+1} - r_{k-1}} \left( \frac{r_k}{r_{k+1}} \right) \sum_{j,m} Y_{jm}(\theta, \varphi)|_{\theta_0, \varphi_0} \delta U_{jm}^{k+1}, \quad (\text{A5})$$

$$\delta \mathcal{W}^{(C-)} = -\frac{\mu_k \Delta u \Delta A}{r_0} \sin 2\delta \sin \alpha \frac{r_k}{r_{k+1} - r_{k-1}} \left( \frac{r_k}{r_{k-1}} \right) \sum_{j,m} Y_{jm}(\theta, \varphi)|_{\theta_0, \varphi_0} \delta U_{jm}^{k-1}, \quad (\text{A6})$$

$$\delta \mathcal{W}^{(D+)} = -\frac{\mu_k \Delta u \Delta A}{r_0} \cos 2\delta \sin \alpha \frac{r_k}{r_{k+1} - r_{k-1}} \left( \frac{r_k}{r_{k+1}} \right) \sum_{j,m} \left[ \sin \Theta \frac{\partial Y_{jm}^*(\theta, \varphi)}{\partial \theta} + \cos \Theta \frac{1}{\sin \theta} \frac{\partial Y_{jm}^*(\theta, \varphi)}{\partial \varphi} \right]_{\theta_0, \varphi_0} \delta V_{jm}^{k+1}, \quad (\text{A7})$$

$$\delta \mathcal{W}^{(D-)} = \frac{\mu_k \Delta u \Delta A}{r_0} \cos 2\delta \sin \alpha \frac{r_k}{r_{k+1} - r_{k-1}} \left( \frac{r_k}{r_{k-1}} \right) \sum_{j,m} \left[ \sin \Theta \frac{\partial Y_{jm}^*(\theta, \varphi)}{\partial \theta} + \cos \Theta \frac{1}{\sin \theta} \frac{\partial Y_{jm}^*(\theta, \varphi)}{\partial \varphi} \right]_{\theta_0, \varphi_0} \delta V_{jm}^{k-1}, \quad (\text{A8})$$

$$\delta \mathcal{W}^{(D+T)} = \frac{\mu_k \Delta u \Delta A}{r_0} \cos 2\delta \sin \alpha \frac{r_k}{r_{k+1} - r_{k-1}} \left( \frac{r_k}{r_{k+1}} \right) \sum_{j,m} \left[ \sin \Theta \frac{1}{\sin \theta} \frac{\partial Y_{jm}^*(\theta, \varphi)}{\partial \varphi} - \cos \Theta \frac{\partial Y_{jm}^*(\theta, \varphi)}{\partial \theta} \right]_{\theta_0, \varphi_0} \delta W_{jm}^{k+1}, \quad (\text{A9})$$

$$\delta \mathcal{W}^{(D-T)} = -\frac{\mu_k \Delta u \Delta A}{r_0} \cos 2\delta \sin \alpha \frac{r_k}{r_{k+1} - r_{k-1}} \left( \frac{r_k}{r_{k-1}} \right) \sum_{j,m} \left[ \sin \Theta \frac{1}{\sin \theta} \frac{\partial Y_{jm}^*(\theta, \varphi)}{\partial \varphi} - \cos \Theta \frac{\partial Y_{jm}^*(\theta, \varphi)}{\partial \theta} \right]_{\theta_0, \varphi_0} \delta W_{jm}^{k-1}. \quad (\text{A10})$$

$$\delta \mathcal{W}^{(E)} = \frac{\mu_k \Delta u \Delta A}{r_0} \sin \delta \cos \alpha \sum_{j,m} \left[ (\sin^2 \Theta - \cos^2 \Theta) \frac{1}{\sin \theta} \frac{\partial^2 Y_{jm}^*(\theta, \varphi)}{\partial \theta \partial \varphi} + (\sin^2 \Theta - \cos^2 \Theta) \frac{\partial}{\partial \theta} \left( \frac{1}{\sin \theta} \frac{\partial Y_{jm}^*(\theta, \varphi)}{\partial \varphi} \right) + 2 \sin \Theta \cos \Theta \left( -\frac{\partial^2 Y_{jm}^*(\theta, \varphi)}{\partial \theta^2} + \frac{1}{\sin^2 \theta} \frac{\partial^2 Y_{jm}^*(\theta, \varphi)}{\partial \varphi^2} + \frac{1}{\tan \theta} \left[ \frac{\partial Y_{jm}^*(\theta, \varphi)}{\partial \theta} - \frac{1}{\sin \theta} \frac{\partial Y_{jm}^*(\theta, \varphi)}{\partial \varphi} \right] \right) \right]_{\theta_0, \varphi_0} \delta V_{jm}^k, \quad (\text{A11})$$

$$\delta\mathcal{W}^{(ET)} = \frac{\mu_k \Delta u \Delta A}{r_0} \sin \delta \cos \alpha \sum_{j,m} \left[ (\sin^2 \Theta - \cos^2 \Theta) \frac{\partial^2 Y_{jm}^*(\theta, \varphi)}{\partial \theta^2} + (\cos^2 \Theta - \sin^2 \Theta) \frac{1}{\sin^2 \theta} \frac{\partial^2 Y_{jm}^*(\theta, \varphi)}{\partial \varphi^2} + 2 \sin \Theta \cos \Theta \right. \\ \left. \times \frac{\partial}{\partial \theta} \left( \frac{1}{\sin \theta} \frac{\partial Y_{jm}^*(\theta, \varphi)}{\partial \varphi} \right) \right]_{\theta_0, \varphi_0} \delta W_{jm}^k, \quad (\text{A12})$$

$$\delta\mathcal{W}^{(F+)} = \frac{\mu_k \Delta u \Delta A}{r_0} \cos \delta \cos \alpha \frac{r_k}{r_{k+1} - r_{k-1}} \left( \frac{r_k}{r_{k+1}} \right) \sum_{j,m} \left[ \sin \Theta \frac{1}{\sin \theta} \frac{\partial Y_{jm}^*(\theta, \varphi)}{\partial \varphi} - \cos \Theta \frac{\partial Y_{jm}^*(\theta, \varphi)}{\partial \theta} \right]_{\theta_0, \varphi_0} \delta V_{jm}^{k+1}, \quad (\text{A13})$$

$$\delta\mathcal{W}^{(F-)} = -\frac{\mu_k \Delta u \Delta A}{r_0} \cos \delta \cos \alpha \frac{r_k}{r_{k+1} - r_{k-1}} \left( \frac{r_k}{r_{k-1}} \right) \sum_{j,m} \left[ \sin \Theta \frac{1}{\sin \theta} \frac{\partial Y_{jm}^*(\theta, \varphi)}{\partial \varphi} - \cos \Theta \frac{\partial Y_{jm}^*(\theta, \varphi)}{\partial \theta} \right]_{\theta_0, \varphi_0} \delta V_{jm}^{k-1}. \quad (\text{A14})$$

$$\delta\mathcal{W}^{(F+T)} = \frac{\mu_k \Delta u \Delta A}{r_0} \cos \delta \cos \alpha \frac{r_k}{r_{k+1} - r_{k-1}} \left( \frac{r_k}{r_{k+1}} \right) \sum_{j,m} \left[ \sin \Theta \frac{\partial Y_{jm}^*(\theta, \varphi)}{\partial \theta} + \cos \Theta \frac{1}{\sin \theta} \frac{\partial Y_{jm}^*(\theta, \varphi)}{\partial \varphi} \right]_{\theta_0, \varphi_0} \delta W_{jm}^{k+1}, \quad (\text{A15})$$

$$\delta\mathcal{W}^{(F-T)} = -\frac{\mu_k \Delta u \Delta A}{r_0} \cos \delta \cos \alpha \frac{r_k}{r_{k+1} - r_{k-1}} \left( \frac{r_k}{r_{k-1}} \right) \sum_{j,m} \left[ \sin \Theta \frac{\partial Y_{jm}^*(\theta, \varphi)}{\partial \theta} + \cos \Theta \frac{1}{\sin \theta} \frac{\partial Y_{jm}^*(\theta, \varphi)}{\partial \varphi} \right]_{\theta_0, \varphi_0} \delta W_{jm}^{k-1}, \quad (\text{A16})$$

where superscripts (A–D) and (E–F) denote dip-slip and strike-slip components, respectively, and  $\Delta u$  and  $\Delta A$  are the slip and the area of the fault for prescribing moment magnitude, and  $\Theta$ ,  $\delta$  and  $\alpha$  are the strike, dip and rake angles, respectively. The variations with superscripts including + (–) are imposed at the radial distance  $r^{k+1}$  ( $r^{k-1}$ ) and those excluding  $\pm$  are given at  $r^k$ . [In Tanaka *et al.* (2009), some terms were missing from the representations of  $\delta\mathcal{W}^{(B, E, ET)}$ .] The variation for double-couple forces corresponding to a point dislocation with an arbitrary strike, dip and rake angles is represented by combining the above variations (eqs A2–A16), and is considered in  $\delta\mathcal{W}^{i+1}$  on the right-hand side of the variational equality (eq. 16).

## APPENDIX B: MASS REDISTRIBUTION BY OCEAN BOTTOM DEFORMATION

The theoretical gravity changes presented in this study are corrected for the effects of mass redistribution of the ocean mass as follows: When considering only the vertical motion of the ocean floor, the additional potential change at an observation site with angular variables  $\Omega$  can be written as

$$\phi(\Omega) = Ga^2 \rho_w \int d\Omega' [\Delta\phi(\Omega')/g_0 - \mathbf{u}(\Omega') \cdot \mathbf{e}_r] / r, \quad (\text{B1})$$

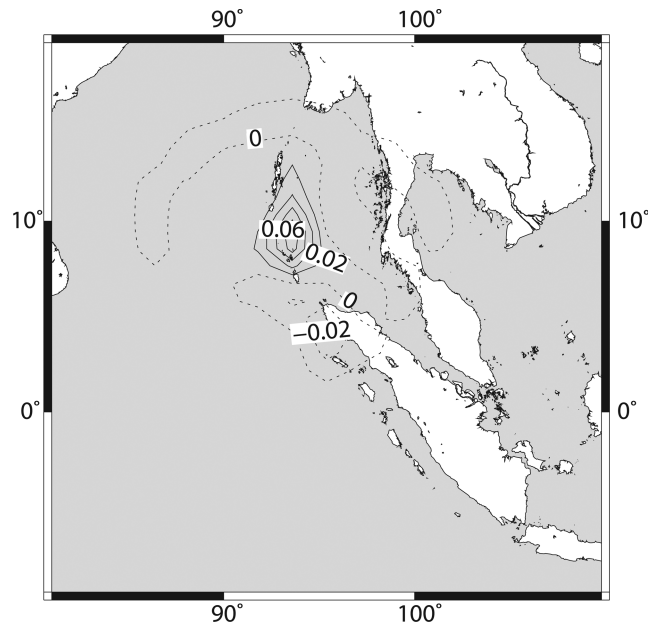


**Figure B1.** The gravity change due to the mass redistribution of the ocean mass, caused by the horizontal motion of the ocean bottom. The units are  $\mu\text{Gal}$ , the contour interval is  $0.01 \mu\text{Gal}$  and dotted lines denote negative changes.

where  $\rho_w$ ,  $a$ ,  $\Omega'$  and  $r$  denote the density of water ( $=1000 \text{ kg m}^{-3}$ ), the radius of the Earth, angular variables where the ocean mass increment is placed and the distance between the observation site and the mass increment.  $\Delta\phi$  is the potential change due to the solid Earth deformation, which is negligible compared with the latter term. If the ocean floor is not flat, horizontal deformation pushes away the water so that

$$Ga^2\rho_w \int d\Omega' [\mathbf{u}_h(\Omega') \cdot \nabla_h H(\Omega')] / r \quad (\text{B2})$$

is added to eq. (B1), where the subscript  $h$  and  $H$  represent the derivation along the surface and the ocean bottom topography. The topography data can be obtained from the web site of the University of Alaska (<http://www.gina.alaska.edu/data/topo-dem-bathymetry>). In eq. (B2), the horizontal displacement can be expanded by spherical harmonics. By numerically computing  $\nabla_h H$  and the coefficient of the spherical harmonics, eq. (B2) takes the form of Fourier transform, which gives the spherical harmonic coefficients of the potential on the left-side hand. The coefficients can be computed by an FFT.

Fig. C1 shows the gravity change computed from eq. (B2). The change is observed near the epicentre where the horizontal displacement and the tilt of the topography is steep along the direction of the displacement. However, the change is smaller than  $0.1 \mu\text{Gal}$  when the same spatial filter and the cut-off degree is applied (Section 3).

### APPENDIX C: GRAVITY CHANGE DUE TO THE 28 MARCH 2005 NIAS EARTHQUAKE

Fig. C1 shows the gravity change caused by the instantaneous elastic response to the 2005 Nias event. The fault model described in Banerjee *et al.* (2007) is adopted. The amplitude of the change does not exceed  $\sim 1.3 \mu\text{Gal}$ , which is significantly smaller than the gravity change due to afterslip and viscoelastic relaxation of the 2004 Sumatra–Anadaman event.

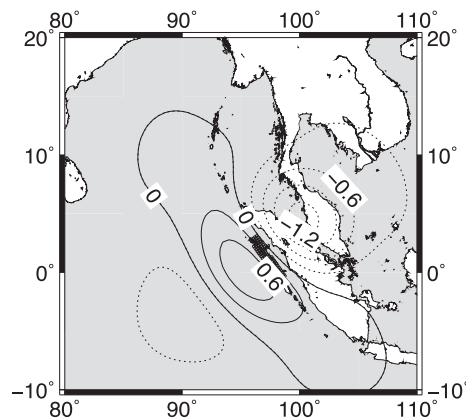


**Figure C1.** The theoretically estimated coseismic gravity change due to the 2005 March 28 Nias earthquake. The units are  $\mu\text{Gal}$ , and the contour interval is  $0.3 \mu\text{Gal}$ . The dotted curves denote that the change is negative.